Colon-Targeting pH-Responsive Bletilla striata Polysaccharide Coacervate Microdroplets for Ulcerative Colitis Therapy via Macrophage Reprogramming

Qiantao Zhang
Lai Chai
Hui Liu
Xueer Hu
Yujing Niu
Hongli Cao
Xin Rao
Mingyuan Zhou
Yuchi Chen
Xiaoqing Ye
Fangmei Zhou
Zhishan Ding
Bingqi Zhu
bingqizhu@163.com

Research Article

Keywords: Ulcerative colitis, Bletilla striata polysaccharide, Macrophage reprogramming

Posted Date: June 30th, 2026

DOI: https://doi.org/10.21203/rs.3.rs-10116278/v1

Additional Declarations: No competing interests reported.

Version of Record: A version of this preprint was published at Journal of Nanobiotechnology on July 20th, 2026. See the published version at https://doi.org/10.1186/s12951-026-04824-1.

Colon-Targeting pH-Responsive *Bletilla striata* Polysaccharide Coacervate Microdroplets for Ulcerative Colitis Therapy via Macrophage Reprogramming

Qiantao Zhang[a, 1], Lai Chai [a, 1], Hui Liu [a, 1], Xueer Hu[a], Yujing Niu[a], Hongli Cao[a], Xin Rao[a], Mingyuan Zhou[a], Yuchi Chen[a], Xiaoqing Ye[a], Fangmei Zhou[a], Zhishan Ding[a, *] and Bingqi Zhu[a, *]

[a] School of Medical Technology and Information Engineering, Zhejiang Chinese Medical University, Hangzhou, 310053, Zhejiang, the People's Republic of China.

1 The authors contribute equally

*Corresponding author. Bingqi Zhu's E-mail address: bingqizhu@163.com.

Zhishan Ding's E-mail address: dzszjtcm@163.com.

Abstract

Ulcerative colitis (UC) is an immune-mediated chronic inflammatory bowel disease that severely impairs patients' quality of life. Current clinical treatments urgently require efficient colon-targeted drug delivery systems to overcome the limitations of traditional therapeutics, such as poor lesion-targeting efficacy and significant systemic toxicity. Herein, we constructed a novel pH-responsive coacervate microdroplet delivery system based on natural *Bletilla striata* polysaccharide (BSP) for the precise intervention of UC. *In vitro* evaluations demonstrated that this platform exhibits excellent biocompatibility and precise pH-responsive release characteristics, effectively protecting the active ingredients from premature degradation in the upper gastrointestinal tract. *In vivo* imaging further confirmed that after oral administration, these microdroplets can precisely target and be persistently retained at the colonic inflammatory lesions. Mechanistic studies revealed that this system profoundly reprograms macrophage polarization from the pro-inflammatory M1 phenotype to the anti-inflammatory M2 phenotype, synergistically suppressing pro-inflammatory cytokine secretion. Concurrently, the targeted accumulation of BSP effectively scavenged local reactive oxygen species (ROS), promoted mucosal barrier repair by upregulating tight junction proteins, and reshaped the homeostasis of the gut microbiota. In summary, this study not only provides a universal strategy for developing safe and highly efficient natural polysaccharide-based targeted delivery platforms but also lays a rigorous experimental foundation for IBD therapy based on a multi-dimensional "immunity-barrier-microbiota" regulation strategy.

Key words: Ulcerative colitis; *Bletilla striata* polysaccharide; Macrophage reprogramming

1.Introduction:

Ulcerative colitis (UC) represents a prominent global health challenge, defined pathologically by idiopathic inflammation restricted to the colonic mucosa[1]. With a burgeoning patient population approaching five million worldwide, the disease is clinically characterized by a chronic, relapsing-remitting course and debilitating symptoms, including persistent abdominal pain, chronic diarrhea, rectal hemorrhage, and significant weight loss[2]. At present, the complex etiology and underlying molecular mechanisms of UC remain to be fully elucidated, leaving the clinical field without a definitive cure or a universally accepted diagnostic framework[3].

Ulcerative colitis is characterized by alternating cycles of symptomatic flare-ups and periods of remission, necessitating sustained therapeutic intervention to achieve and preserve a stable clinical state[4]. While a range of pharmacological agents—including salicylates, corticosteroids, immunosuppressants, and biological therapies—are standard in clinical practice, their chronic administration is frequently undermined by the development of drug resistance, significant adverse reactions, and a progressive decline in therapeutic response[5]. In response to these clinical bottlenecks, medicinal plants have emerged as a promising alternative, favored for their "multi-component, multi-pathway" mechanisms and superior safety profile[6, 7]. *Bletilla striata* (Thunb.) Reichb. f. is a prominent traditional herb valued for its mild restorative properties and has historically been employed for hemostasis and the repair of ulcers, wounds, and mucosal lesions, serving as a critical component in various classical UC formulations. As the primary bioactive fraction, *Bletilla striata* polysaccharide (BSP) exhibits a broad spectrum of pharmacological activities, encompassing immunomodulatory, anti-inflammatory, anti-tumor, anti-fibrotic, and gastroprotective effects. Current research suggests that BSP and its derived oligosaccharides are highly effective in promoting hemostasis and accelerating wound healing. Moreover, these polysaccharides contribute to UC management by suppressing pro-inflammatory cytokine secretion, fortifying the intestinal epithelial barrier, and recalibrating gut microbiota homeostasis and associated metabolic profiles[8].

As a potent bioactive macromolecule, BSP exhibits significant anti-inflammatory and mucosal-reparative activities. However, its structural integrity is highly sensitive to the hyperacidic gastric environment, where rapid degradation often leads to a precipitous decline in bioavailability following direct oral administration[9]. Similar acid-mediated instability is a common vulnerability among natural glycans, such as those derived from *Poria cocos* and *Tremella fuciformis*; specifically, *Poria cocos* polysaccharide has been shown to undergo complete degradation within a 0.5-hour exposure to simulated gastric fluid[10]. These observations underscore that achieving robust gastric protection remains a pivotal challenge for natural polysaccharide-based delivery systems in the management of ulcerative colitis. Such barriers highlight the exigent demand for the engineering of pH-responsive enteric platforms, which can sequester bioactive agents from premature gastric release and ensure precise, targeted accumulation within colonic lesions.

Coacervate microdroplets are typically high-density polyelectrolyte liquids formed through liquid-liquid phase separation of two oppositely charged polymers in a solvent, manifesting as discrete spherical droplets. These coacervates can be facilely fabricated via simple self-assembly in aqueous media using a diverse range of raw materials, characterized by their innate ability to spontaneously sequester both small molecules and biological macromolecules[11, 12]. Unlike conventional delivery vehicles—such as emulsions, micelles, lipid nanoparticles, and liposomes—coacervate microdroplets demonstrate a unique capacity for the potent enrichment of diverse cargoes regardless of their hydrophobicity, molecular weight, or isoelectric point, achieving exceptionally high loading efficiencies[11]. However, coacervates are inherently prone to aggregation, which challenges the maintenance of a stable, uniformly dispersed state over extended periods. This instability necessitates the integration of lipid molecules, nanomaterials, or cell membranes to enhance their structural robustness[13]. Eudragit S100 (EU S100) is a widely utilized pH-responsive enteric coating material that dissolves exclusively in environments where pH > 7; it effectively shields orally administered, unstable therapeutics from the harsh gastric milieu while enabling precise targeted delivery to the colon[14, 15]. Consequently, the

development of an innovative oral coacervate-based delivery system is imperative—one that leverages the spontaneous sequestration and high-loading capacity of coacervates while incorporating a protective coating to achieve colon-specific targeting and sustained drug release for the management of UC.

In this study, we constructed DEAE-Dextran/PSS coacervate microdroplets (Coac) utilizing diethylaminoethyl-dextran hydrochloride and sodium polyphenylene sulfonate, into which BSP was incorporated via spontaneous enrichment to form BSP@Coac. To enhance the structural stability of the coacervates against gastric acid and pepsin and to achieve precise colon-targeted delivery, BSP@Coac was encapsulated within the pH-sensitive enteric coating material Eudragit S100, yielding the BSP@EU-Coac platform. In vitro evaluations demonstrate that this platform possesses exceptional biocompatibility and a sophisticated pH-responsive release profile, enabling the site-specific enrichment and sustained delivery of bioactive components. Furthermore, the system effectively inhibits the excessive polarization of macrophages toward the pro-inflammatory M1 phenotype while promoting their transition toward the reparative M2 phenotype, thereby equilibrating the secretion of pro- and anti-inflammatory mediators. In a murine model of UC, BSP@EU-Coac significantly attenuated colonic levels of inflammatory cytokines and ROS, markedly upregulated the expression of intestinal tight junction proteins, and enhanced the abundance of beneficial gut microbiota. These results collectively indicate that BSP@EU-Coac achieves comprehensive therapeutic efficacy in UC stress, repair of intestinal epithelial damage, and regulation of gut microbiota homeostasis.

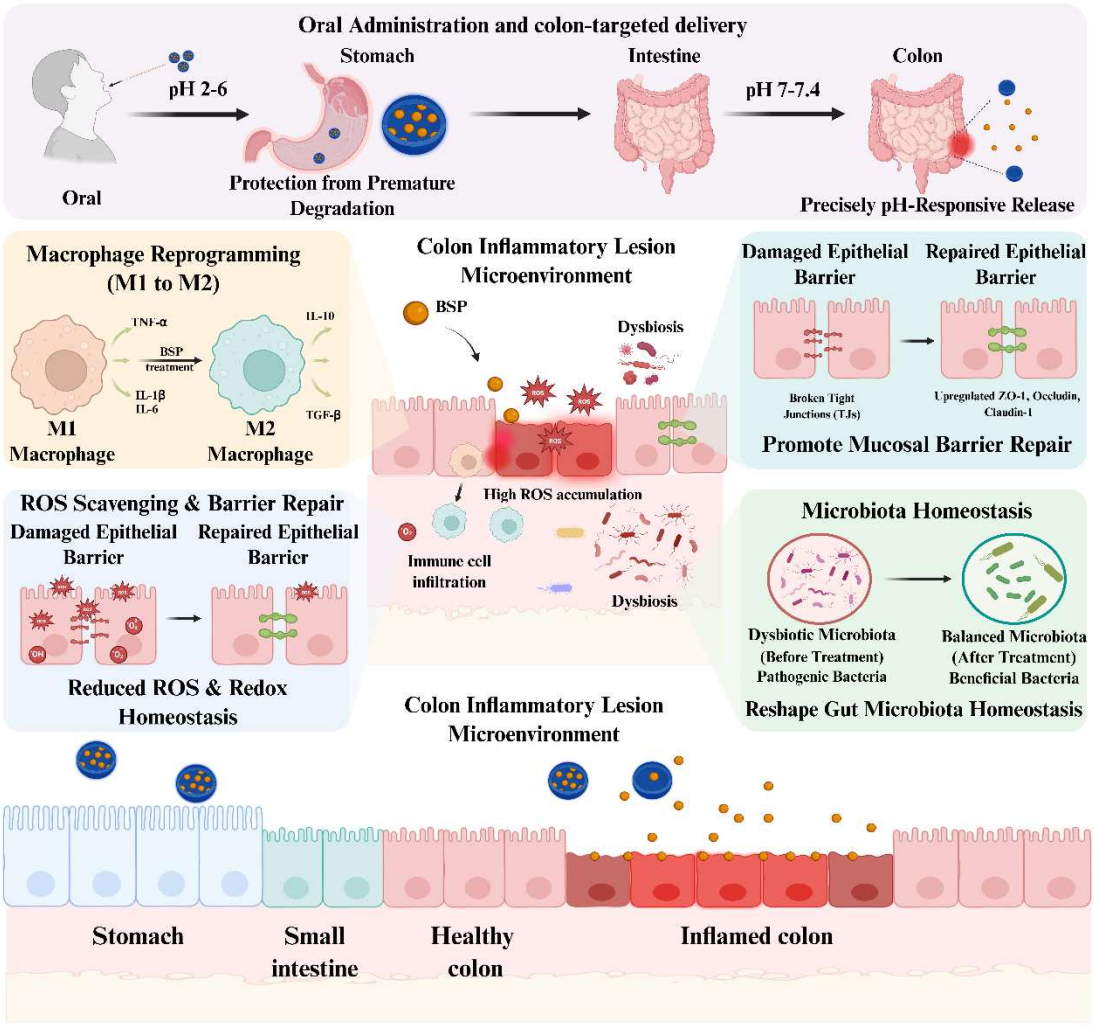

Scheme 1. Schematic overview of the colon-targeted pH-responsive BSP@EU-Coac delivery system for ulcerative colitis therapy.

2.Materials and methods

2.1. Materials

Diethylaminoethyl-dextran hydrochloride (DEAE-Dextran), sodium polyphenylene sulfonate (PSS, Mw 70 000), Eudragit S100, hydrogen peroxide, Pepsin were bought from Macklin (Shanghai, China). BSP, Sephadex G-50 were purchased from Shanghai Yuanye Biotechnology Co., Ltd. (Shanghai, China). Malondialdehyde (MDA), Superoxide Dismutase (SOD), and reduced glutathione (GSH) kits were purchased from Abbkine (Wuhan, China). 5-(4,6 - Dichlorotriazinyl)aminofluorescein (5-DTAF) was obtained from Shanghai Aladdin Biochemical Technology Co., Ltd.

(Shanghai, China). The CCK-8 cell counting kit, ROS detection kit, bacterial viability/cytotoxicity staining kit (DMAO/PI) and 4′,6-diamidino-2′-phenylindole (DAPI) were purchased from Shanghai Beyotime Biotechnology Co., Ltd. (Shanghai, China). Dextran sulfate sodium salt (DSS, MW: 36000-50000) was brought from MeliunBio (Liaoning, China). Dulbecco's Modified Eagle Medium (DMEM), fetal bovine serum, penicillin, and streptomycin were purchased from Gibco (Waltham, MA, USA). Antibodies against CD16/32, PE-CD86, APC-CD206, and F4/80 were sourced from BioLegend (USA). Anti-mouse CD206 and anti-mouse CD86 were purchased from Abcam (UK). Goat anti-rabbit Cora Lite Plus 592, goat anti-rabbit Cora Lite Plus 488, goat anti-mouse Cora Lite Plus 488, HRP-labeled goat anti-mouse IgG (H+L), and HRP-labeled goat anti-rabbit IgG (H+L) were obtained from Wuhan Sanying Biotechnology Co., Ltd. (Proteintech, Wuhan, China).

2.2 Construction of Coacervate Microdroplets

2.2.1 Preparation of BSP@EU-Coac

Following a previously reported approach, coacervate microdroplets were engineered through the liquid-liquid phase separation of DEAE-Dextran and PSS[16]. BSP was dissolved in deionized water with a concentration of 5 mg mL^{-1}. First, different volumes of BSP solutions were added to 600 μL PSS solution (5 mg mL^{-1}) and shaken slightly. Then, 1.2 mL DEAE-Dextran solution (5 mg mL^{-1}) mixed thoroughly with the compounds and stood for 4 h to prepare BSP@Coac of different mass ratios (BSP: Coac, 1:40, 1:20, 1:10, 1:5). The prepared BSP@Coac was centrifuged at 1000 g for 5 min and washed twice with PBS (pH 7.2), then resuspended with PBS (pH 5.5). The EU S100 suspension was added slowly to the BSP@Coac to produce BSP@EU-Coac.

2.2.2 Material Characterization

BSP@EU-Coac was diluted to 0.5 mg mL^{-1}. The morphological characteristics were observed using transmission electron microscopy (TEM), while the zeta potential and functional groups were determined via dynamic light scattering (DLS) and Fourier-transform infrared (FTIR) spectroscopy, respectively.

2.2.3 Encapsulation Efficiency and Drug Loading

The encapsulation efficiency (EE) and drug loading (DL) of BSP were determined using Phenol-sulfuric acid method and UV-Vis Spectroscopy.

To achieve precise quantification of the BSP concentration, a standard curve was generated using the phenol–sulfuric acid colorimetric method. A concentration gradient of BSP standard solutions was prepared in deionized water. For each concentration, a 20 μL aliquot was blended with 20 μL of 5% (w/v) aqueous phenol solution, followed by the rapid injection of 100 μL of concentrated sulfuric acid. The reaction mixture was homogenized via vortexing and incubated at 90°C for 15 min to facilitate complete chromogenic development. The absorbance of the resulting orange-yellow complex was determined at 490 nm utilizing a UV–vis spectrophotometer. To quantify the drug content, a defined aliquot of the BSP@EU-Coac suspension was harvested and subsequently mixed with a saturated NaCl solution. The high-salinity environment effectively shields the electrostatic interactions between DEAE-Dextran and PSS, facilitating the complete dissociation of the coacervate framework. The resulting mixture was centrifuged at 1000 g for 5 min, and the supernatant was collected. The BSP concentration within the supernatant was then determined according to the aforementioned phenol-sulfuric acid assay. EE and DL were calculated using the following established equations:

$$\text{EE (\%)} = \frac{\mathrm{M0}}{\mathrm{M1}} \times 100\%$$

$$\text{DL (\%)} = \frac{\mathrm{M0}}{\mathrm{M}} \times 100\%$$

Where M0 represents the mass of BSP loaded within the coacervates, M1 is the total mass of BSP initially added, and M denotes the total mass of the BSP-loaded coacervate system.

2.2.4 Drug Release Behavior Study In Vitro

The dialysis method was used to study the release of BSP in simulated gastrointestinal fluid. In particular, PBS with different pH was used for the medium as simulated gastric fluid (SGF, pH 1.2), simulated small intestine fluid (SIF, pH 6.8), and simulated colonic fluid (SCF, pH 7.4). 1 mL BSP@Coac or BSP@EU-Coac solution

was added to the dialysis bags (MWCO 14000), respectively. The dialysis bags were placed in centrifuge tubes containing 10 mL releasing medium and stirred at 100 rpm at 37 °C. Releasing medium was replaced according to the following time sequence: 0–2 h (SGF), 2–6 h (SIF), 6–96 h (SCF). At different predetermined time points, 2 mL of medium was collected and determined by the phenol-sulfuric acid method for drug release measurement.

2.3 Synthesis of 5-DTAF-Labeled BSP

2.3.1 Fluorescent labeling

The fluorescent labeling procedures were adapted from previous studies[17, 18]. For 5-DTAF labeling, 20 mg of BSP was reacted with 3 mg of 5-DTAF in 10 mL carbonate buffer (pH = 9.5) under light-protected conditions at room temperature for 24 h, then transferred to 4 °C for an additional 24 h. The labeled product was purified by dialysis and Sephadex G50 gel column chromatography (2.5 × 50 cm), followed by freeze-drying to obtain FBSP.

2.3.2 Fluorescence spectral analysis

FBSP, 5-DTAF were prepared at appropriate concentrations in fluorescence cuvettes. Spectra were recorded with excitation/emission settings of 488/525 nm using a fluorescence spectrophotometer (F-7000, Hitachi, Japan).

2.3.3 UV–visible spectral analysis

Protein content in aqueous solutions (5 mg mL^{-1}) of 5-DTAF, FBSP was qualitatively assessed over 190–350 nm using a Nanodrop One UV–Vis spectrophotometer (Thermo Fisher Scientific, Waltham, MA, USA).

2.3.4 FT-IR spectroscopy

Functional groups of 5-DTAF, FBSP were analyzed by FT-IR spectroscopy using the KBr pellet method (0.5 mg sample/100 mg KBr). Spectra were recorded over 4000–400 cm^{-1} with a Fourier transform infrared spectrometer (Nicolet iS50, Thermo Fisher Scientific, Massachusetts, USA).

2.4 Biocompatibility Test

2.4.1 Cytotoxicity (CCK-8 Assay)

Caco-2 or RAW264.7 cells were seeded in 96-well plates (1×10^5 cells/well). After adhesion, BSP, BSP@Coac, BSP@EU-Coac were added and incubated for 24 h. 10 μL CCK-8 reagent was added, incubated in dark for 1 h, and absorbance (OD value) was measured at 450 nm.

2.4.2 Cell Viability (Live/Dead Staining)

Cells were seeded and treated with BSP, BSP@Coac, BSP@EU-Coac as previously described. After twenty-four hours, the medium was removed and replaced with a Live/Dead working solution prepared according to the manufacturer's instructions. Following a thirty-minute incubation in the dark, the cells were washed three times with PBS. Finally, fluorescent images were captured using confocal microscopy.

2.5 Immunomodulatory Properties

2.5.1 In Vitro Promotion of Macrophage Polarization

BMDMs were isolated, cultured, and polarization-induced as described in reference[19, 20]. Briefly, sterile bone marrow cells from 6-week-old mouse femurs were differentiated into BMDMs in medium with L929 cell-conditioned medium; mature BMDMs were collected on day 7. After overnight seeding, cells were grouped: drug-treated cells were pretreated with coacervate microdroplets for 2 h, then co-stimulated with LPS (250 ng mL^{-1}) and IFN-γ (30 ng mL^{-1}) for 12 h; model group only received LPS/IFN-γ stimulation.

Post-stimulation, cells were harvested for phenotypic analysis. For flow cytometry, cells were dark-stained with PE-anti-CD86 and APC-anti-CD206 for 30 min, washed with PBS and resuspended for further analysis. For immunofluorescence, fixed/permeabilized cells were incubated with anti-CD86/CD206 primary antibodies (1:400, Proteintech) at 4 °C overnight, washed with PBST, incubated with CoraLite Plus 488 secondary antibody (1:1000, Proteintech), mounted with DAPI antifade

medium, imaged via inverted fluorescence microscopy, and fluorescence intensity quantified by ImageJ.

2.5.2 In Vitro Anti-inflammatory Experiment

BMDM cells were seeded into 12-well plates at a density of 3×10^5 cells per milliliter. After allowing the cells to adhere overnight, they were divided into three groups. The control group was cultured in complete DMEM. The model group was treated with a combination of 1 μg mL^{-1} LPS and 30 ng mL^{-1} IFN-γ. The experimental group first received a two-hour pretreatment with the hydrogel extract, followed by the same LPS and IFN-γ stimulation. All groups were incubated overnight. Subsequently, the cells were washed with DMEM and harvested for RNA extraction to analyze the expression of inflammation-related mRNAs. The primer sequences used in this analysis are provided in Supporting Information Table S1.

2.6 Cell Scratch Assay

Cell migration under different drug treatments was assessed using a scratch-wound healing assay. Caco-2 were seeded in 24-well plates (3×10^4 cells/well) and cultured until approximately 80% confluent. A scratch was made in the monolayer using a sterile 200 μL pipette tip, followed by three washes with DMEM to remove detached cells. Fresh medium containing hydrogel extract was then added. Images of the scratch were captured at 0 h and 24 h using an inverted microscope. The scratch areas at 0 h (A_0) and 24 h (A_1) were measured using ImageJ.

$$\text{Migration Rate (\%)} = \frac{A_0 - A_1}{A0} \times 100\%$$

2.7 Intracellular ROS Scavenging Assay

The intracellular ROS-scavenging capacities of BSP, BSP@Coac and BSP@EU-Coac were detected using commercial kits. Raw 264.7 cells were seeded into 12-well plates at a density of 1×10^5 cells/cm^2 and stimulated with 1 μg mL^{-1} LPS for 12 h to induce ROS production. After removing the culture medium, the experimental groups were treated with different hydrogel extracts for 24 h, washed with PBS, and incubated with 10 μM DCFH-DA at 37 °C in the dark for 30 min. Finally, the cells were analyzed

by flow cytometry and inverted fluorescence microscopy.

2.8 Animals

C57BL/6 (6–8 weeks old, 20–25g) mice were used in this study. All animal experiments were approved by the Animal Ethical and Welfare Committee of Zhejiang Chinese Medical University (approval code: IACUC- 20250616-10). Mice were housed under standard laboratory conditions and acclimated for 1 week before experiments. The animal use license is SYXK (Zhejiang) 2021-0012.

2.9 Biodistribution Evaluation In Vivo

FBSP was used as a fluorescent tracer for distribution research. The mice were fed ad libitum with 3 % DSS (W/V) for 7 days to establish the UC model. Then, the mice were randomly divided into four groups, as follows: free 5-DTAF, FBSP, FBSP@Coac, or FBSP@EU-Coac. After oral administration, in vivo fluorescence imaging of mice was performed at 1, 6, 12, and 24 h. At 1, 6, 12, and 24 h, the mice were sacrificed to obtain ex vivo fluorescence imaging of tissues, blood, and entire gastrointestinal tract.

2.10 Therapeutic Evaluation In Vivo

Mice were randomly divided into six groups. During the experiment, Mice were given 4 g kg^{-1} d^{-1} DSS for 6 days and treated with BSP at 5 mg kg^{-1} d^{-1} or 5-ASA at 200 mg kg^{-1} d^{-1} orally from day 4 to day 9. The weights of mice were recorded every day. The health status of mice was applied with the disease activity index (DAI) for comprehensive evaluation. On day 10, all groups of mice were collected with blood and feces, and then sacrificed after being weighed. Then, the state of colons was observed and their lengths were measured. Finally, the colons and major organs were collected and weighed. The collected colons were divided into three segments for H&E, IHC, AB-PAS, immunofluorescence staining, and qPCR analysis.

2.11 16S rDNA Gene Sequencing Analysis 16S rRNA

The total DNA of mouse feces was extracted for PCR amplification in the V3-V4

hypervariable region of 16S rDNA. Based on the amplification results, a library of bacterial gene was established. Comparing the sequence with the bacterial gene library, the species abundance and composition of the bacterial community were analyzed.

2.12 In Vivo Safety Evaluation

To evaluate in vivo safety of oral formulations, the organ index (g/g) was obtained by dividing the weight of main organs by body weight. Simultaneously, a series of blood biochemical indicators, including blood urea nitrogen (BUN), blood creatinine (Cre), aspartate aminotransferase (AST), alanine aminotransferase (ALT) were detected. The main organs were cut for H&E staining to monitor histopathological changes.

2.13 Statistical analysis

All data are presented as the mean ± standard deviation of at least three independent experiments. The normality of the sample distribution was tested using the Shapiro-Wilk normality test. Statistical significance for all comparative studies in this research was assessed using GraphPad Prism (version 9.2.0). For statistical analysis comparing multiple groups, one-way Analysis of Variance (ANOVA) was used to compare statistical differences among groups. In the figure captions, "ns" indicates no statistically significant difference ($p > 0.05$), "*", "**" and "***" indicate $p < 0.05$, $p < 0.01$ and $p < 0.001$, respectively.

3. Results and Discussion

3.1 Construction of BSP@Coac

Polyelectrolyte coacervate microdroplets (Coac) were fabricated via spontaneous liquid-liquid phase separation induced by the electrostatic assembly of polycationic DEAE-dextran hydrochloride and polyanionic sodium polyphenylene sulfonate (PSS) in aqueous media, according to previously established protocols [16]. Given the intrinsic physicochemical properties of BSP as a natural biomacromolecule, we systematically explored the drivers governing the formation of BSP@Coac by examining a library of

samples across a BSP: Coac mass ratio range of 1:1–1:40 and concentration range of 1–5 mg mL^{-1}. As illustrated by the turbidity contour map (Fig. 1A), both the mass ratio and concentration significantly modulated the efficiency of coacervate formation, with the system reaching peak turbidity at a ratio of 1:10 and a BSP concentration of 3 mg mL^{-1}.

Furthermore, the EE and DL of BSP within the coacervates were systematically evaluated using the phenol-sulfuric acid method across a mass ratio range from 1:1 to 1:40 (BSP: Coac). Our results indicated that as the BSP-to-Coac ratio increased from 1:40 to 1:10, both DL and EE exhibited a synchronized upward trend, reaching maximum values of 9.29±0.93% and 85.03±3.66%, respectively. Although the DL continued to increase in the 1:1 and 1:5 groups, a significant decline in EE was observed, suggesting that the loading capacity of Coac for BSP had reached saturation (Fig. 1B, C). Thus, a BSP-to-Coac mass ratio of 1:10 at a BSP concentration of 3 mg mL^{-1} was selected as the optimal formulation for all subsequent studies, striking a balance between encapsulation efficiency and material utilization efficiency.

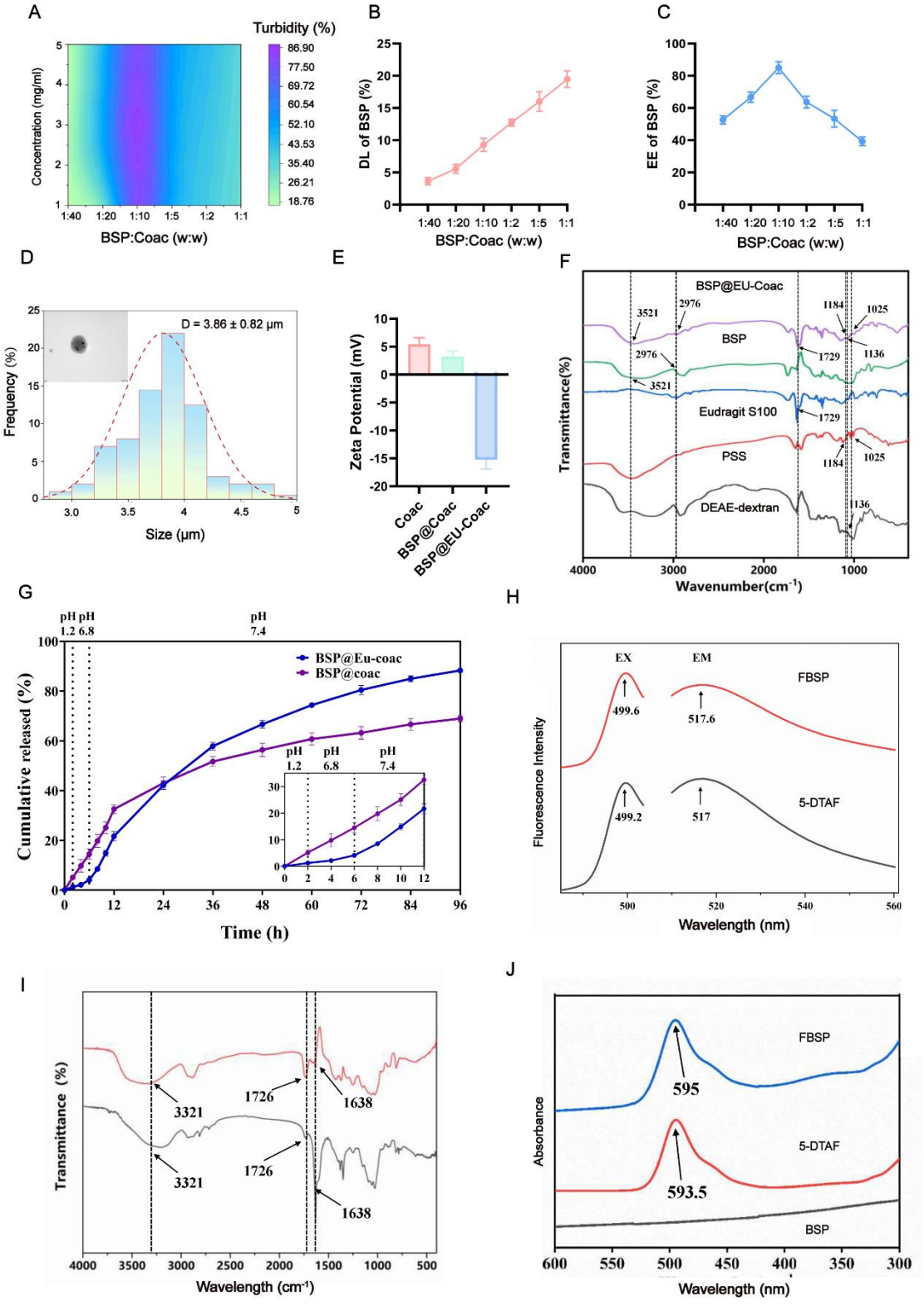

Fig.1 Physicochemical characterization, functional evaluation, and fluorescent labeling of the BSP-loaded coacervate system. (A) Turbidity contour map of the coacervate system. (B, C) DL and EE of BSP across varying mass ratios. (D) Size distribution histogram of BSP@EU-Coac microdroplets. (E) Evolution of zeta potential during the

stepwise assembly of Coac, BSP@Coac, and BSP@EU-Coac. (F) FTIR spectra of DEAE-dextran, PSS, Eudragit S100, BSP. (G) Cumulative in vitro release profiles of BSP from BSP@Coac and BSP@EU-Coac in simulated gastric (pH 1.2), small intestinal (pH 6.8), and colonic (pH 7.4) fluids. The inset highlights the release kinetics during the initial 12 h. (H) Fluorescence excitation (EX) and emission (EM) spectra of free 5-DTAF and the labeled FBSP. (I) FTIR spectra comparing pristine BSP and FBSP to verify the covalent attachment of the fluorophore. (J) UV-Vis absorption spectra of BSP, 5-DTAF, and FBSP.

3.2 Construction and Characterization of BSP@EU-Coac

Owing to the absence of a biomimetic physical barrier, Coac exhibit a high propensity for fusion, aggregation, and precipitation under physiological conditions—instabilities that critically impede their translational potential within complex *in vivo* environments[21]. To address this bottleneck, we report the surface functionalization of Coac using EU S100, a pH-responsive enteric coating material, to engineer a robust and site-specific targeted delivery system.

We systematically investigated the morphological characteristics and surface properties of BSP@EU-Coac. TEM observation (Fig. 1D) revealed that the BSP@EU-Coac microdroplets possessed a distinct spherical morphology with an intact structural boundary, visually confirming the protective effect of the Eudragit S100 shell. Furthermore, as illustrated by the size distribution histogram (Fig. 1D), the final BSP@EU-Coac microdroplets exhibited a well-defined Gaussian distribution with an average hydrodynamic diameter of 3.86±0.82 μm. This micrometer-scale dimension is optimal for facilitating localized retention within the colonic mucosal folds. The successful layer-by-layer assembly and surface functionalization were further corroborated by zeta potential measurements (Fig. 1E). The pristine Coac cores possessed a positive surface charge of approximately + 5.4 mV, which slightly attenuated to + 3.1 mV upon the encapsulation of the natural polysaccharide BSP. Crucially, the subsequent coating with the enteric polymer Eudragit S100 triggered a

distinct charge reversal, resulting in a robust negative potential of - 15.2 mV, thereby confirming the formation of a stable anionic shell[16]. This anionic surface not only confirms the successful formation of the outer shell but also plays a pivotal role in active targeting; it enables the microdroplets to selectively accumulate at the inflamed colonic mucosa via strong electrostatic interactions with the positively charged proteins that are highly overexpressed in the ulcerated lesions[15, 22].

The chemical fingerprints of the composite microdroplets were elucidated via FTIR spectroscopy (Fig. 1F). The spectrum of BSP@EU-Coac retained the characteristic vibrational signatures of all constituent components, indicating successful integration without compromising structural integrity. Specifically, the prominent absorption band at 1729 cm^{-1}, corresponding to the C = O stretching vibration of Eudragit S100, verified the presence of the enteric coating. The broad peaks at 3521 cm^{-1} and 2976 cm^{-1} represent the -OH stretching and C-H vibrations of the BSP and DEAE-dextran frameworks, respectively. Furthermore, the characteristic peaks at 1184 cm^{-1} and 1136 cm^{-1} confirmed the retention of the PSS and DEAE-dextran polyelectrolyte core.

3.3 pH-Triggered Site-Specific Release

To assess the stability and targeting potential of BSP@EU-Coac, *in vitro* release kinetics were monitored across simulated physiological pH gradients (Fig. 1G). The BSP@EU-Coac system demonstrated superior pH-responsive protection compared to the naked BSP@Coac. Under simulated gastric (pH 1.2) and small intestinal (pH 6.8) conditions, the EU-coated microdroplets exhibited negligible premature cargo leakage (less than 20% within the initial 12 h), whereas the naked Coac showed significant early release. Upon transitioning to the simulated colonic environment (pH 7.4), the rapid dissolution of the Eudragit S100 shell facilitated a sustained and controlled release of BSP, achieving a cumulative release of approximately 88.25% by 96 h. This precise, pH-triggered release profile highlights the system's capacity to bypass the upper gastrointestinal tract and ensure maximal drug delivery to the inflamed colonic lesions.

3.4 Fluorescent labeling and characterization of BSP

To facilitate the visualization and spatiotemporal tracking of the polysaccharide, BSP was covalently conjugated with the fluorophore 5-DTAF to synthesize FBSP. The fluorescence excitation (EX) and emission (EM) maxima were determined via spectroscopy: 499.2 nm and 517 nm for free 5-DTAF, and 499.6 nm and 517.6 nm for FBSP, respectively. Both the EX and EM peaks of FBSP exhibited a subtle bathochromic shift (red shift) compared to the precursor 5-DTAF, confirming the successful covalent conjugation of the fluorophore to the BSP backbone (Fig. 1H). Similar shifts have been reported for polysaccharides labeled with fluorophores from *Grifola frondosa* and *Lentinan*[23, 24].

The successful covalent conjugation of 5-DTAF to the BSP backbone was corroborated by FTIR analysis (Fig. 1I). Compared to the pristine BSP, the spectrum of FBSP exhibited distinct new absorption bands at 1638 cm^{-1} which is attributed to the skeletal vibrations of the triazine ring from 5-DTAF. Additionally, the characteristic C=O stretching vibration at 1726 cm^{-1} further confirmed the integration of the fluorophore. The retention of the broad hydroxyl band 3321 cm^{-1} demonstrated that the structural integrity of the BSP framework remained intact post-labeling.

The covalent labeling of BSP with 5-DTAF was further substantiated by UV-Vis absorption spectroscopy (Fig. 1J). While the pristine BSP exhibited negligible absorbance across the visible spectrum, free 5-DTAF displayed a characteristic absorption maximum at 493.5 nm. Following the conjugation reaction, the spectrum of FBSP showed a prominent absorption peak at 495 nm. This subtle bathochromic shift (1.5 nm) relative to the free fluorophore is indicative of the altered electronic environment of the triazine moiety post-conjugation, unequivocally confirming the successful synthesis of the fluorescently labeled polysaccharide.

3.5 Biocompatibility study of the Coacervate Microdroplets

Superior biocompatibility is a prerequisite for biomedical materials. To evaluate the biosafety of the coacervate delivery system for intestinal applications, human

colorectal adenocarcinoma cells (Caco-2), RAW 264.7 macrophages, and bone marrow-derived macrophages (BMDMs) were systematically investigated. CCK-8 assay results (Fig. S1 A-C) revealed that across a broad concentration range, all cell lines maintained high viability (> 80 %) following 24 h of incubation with BSP@EU-Coac, confirming the excellent cytocompatibility of the system. However, at concentrations exceeding 400 μg mL^{-1}, Caco-2 cell viability exhibited a dose-dependent decline to below 52%. This phenomenon is presumably attributed to the high local osmotic pressure generated by the concentrated microdroplet suspension, which may interfere with normal nutrient transport and cellular membrane stability. Importantly, such extreme localized concentrations are unlikely to occur in vivo, as the microdroplets would be substantially diluted by the abundant and dynamic gastrointestinal fluids upon oral administration, further mitigating any concerns regarding material-induced cytotoxicity[25, 26]. Consequently, 10 μg mL^{-1} was selected as the working concentration for subsequent investigations. These findings were further corroborated by Live/Dead staining (Fig. 2A); after 24 h of treatment at 10 μg mL^{-1}, negligible red fluorescence representing dead cells was observed via inverted fluorescence microscopy, underscoring that the system exerts minimal cellular damage at therapeutic dosages.

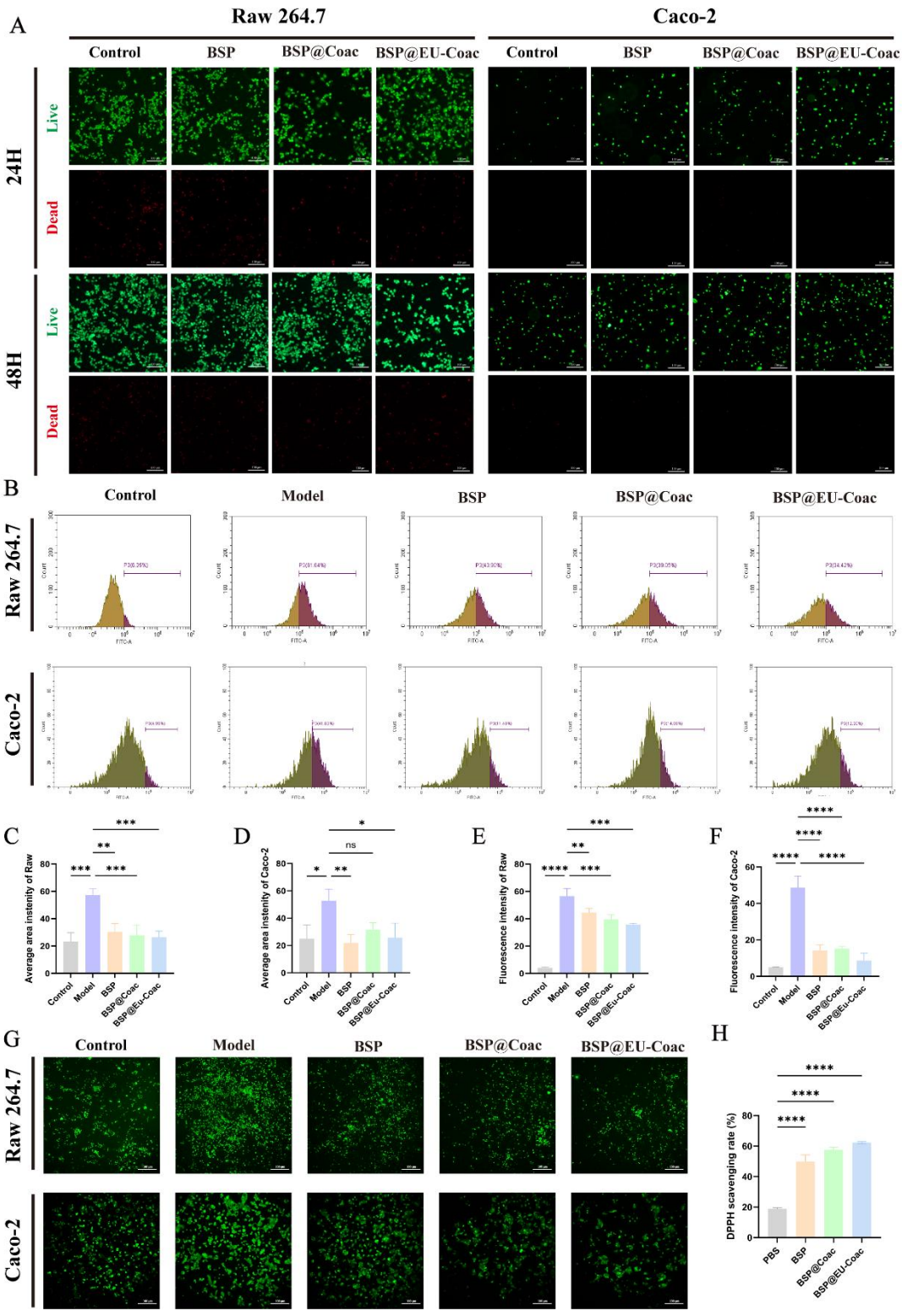

Fig.2 Evaluation of cytocompatibility and intracellular ROS-scavenging capacity. (A) Live/dead cell staining of RAW264.7, Caco-2 cells after co-culture with the coacervates. (B, E, F) Intracellular ROS levels of RAW264.7, Caco-2 cells measured by flow cytometry and corresponding quantification. (C, D, G) Fluorescence microscopy

images of intracellular ROS (green) in RAW 264.7 and Caco-2 cells across different treatment groups and corresponding quantification. n=3. Data are represented as mean values ± SD (n=3). *$p < 0.05$, **$p < 0.01$, ***$p < 0.001$.

3.6 Antioxidant properties of the Coacervate Microdroplets

In the pathological landscape of intestinal inflammation, the aberrant accumulation of ROS instigates oxidative stress, precipitating irreversible damage to the epithelial barrier and fueling inflammatory cascades[27, 28]. Consequently, engineering a therapeutic platform with potent ROS-scavenging capabilities is imperative for restoring redox homeostasis and fostering mucosal repair. Initial cell-free DPPH assays confirmed the robust intrinsic antioxidant capacity of the formulations, revealing that the fully assembled BSP@EU-Coac achieved a DPPH scavenging efficiency of 62.22% (Fig. 2H). To evaluate the antioxidant efficacy of the developed delivery system, intracellular ROS levels were monitored in RAW 264.7 macrophages and Caco-2 cells using the DCFH-DA probe. Visual inspection via inverted fluorescence microscopy (Fig. 2G) revealed intense green fluorescence in the model groups of both cell lines, symptomatic of severe oxidative stress post-induction. Conversely, treatment with BSP@Coac and BSP@EU-Coac markedly attenuated the fluorescence intensity while maintaining cellular morphological integrity. These observations were further substantiated by quantitative analysis (Fig. 2C, D), which showed that the fluorescence area intensity in the BSP@EU-Coac group was reduced by 53.95% and 51.13%, respectively, compared to the model group. Complementary flow cytometric measurements (Fig. 2B, E, F) corroborated these visual findings; the model group exhibited a pronounced rightward peak shift, corresponding to a significant elevation in mean fluorescence intensity (MFI). Notably, BSP@EU-Coac treatment effectively reversed this shift, with intracellular ROS fluorescence intensities dropping to 34.42% and 12.30%, respectively. These levels were substantially lower than those observed in the free BSP and pristine coacervate groups, confirming the robust antioxidant protection conferred by the enteric-coated system against inflammation-induced oxidative damage.

3.7 Coacervate Microdroplets Accelerate Recovery of the Disrupted Colonic Epithelial Barrier

As the colonic epithelial barrier plays a vital function in segregating the underlying mucosa from the hostile colonic lumen, its damage can cause the infiltration of intestinal bacteria and foreign matters into the lamina propria. As a result, inflammatory responses are unnecessarily activated[29, 30]. Hence, repairing the damaged colonic barrier has been recognized as one of the main therapeutic goals against UC[31]. To evaluate the regenerative potential of the BSP-loaded coacervates, we first performed a Caco-2 cell scratch assay to simulate the re-epithelialization process during intestinal injury (Fig. S2A, B). Compared to the Control group, treatment with BSP, BSP@Coac, and BSP@EU-Coac significantly accelerated the migration of Caco-2 cells, achieving over 60% wound closure within 48 h. This enhanced migratory capacity suggests that the delivery system effectively promotes the physical sealing of epithelial denudation.

Beyond physical closure, the mechanical strength and permeability of the barrier are determined by the expression of tight junction (TJ) proteins[29]. As quantified by qPCR (Fig. S2.C-E), the mRNA levels of Occludin, Claudin-1, and ZO-1 were markedly downregulated in the Model group, indicating severe compromise of the junctional complexes. Notably, the administration of BSP-based formulations, particularly the BSP@EU-Coac group, significantly upregulated the expression of these crucial TJ markers, effectively reversing the inflammation-induced barrier defect. Collectively, these findings demonstrate that the coacervate system facilitates synergistic barrier repair by stimulating epithelial cell migration and restoring the molecular framework of tight junctions.

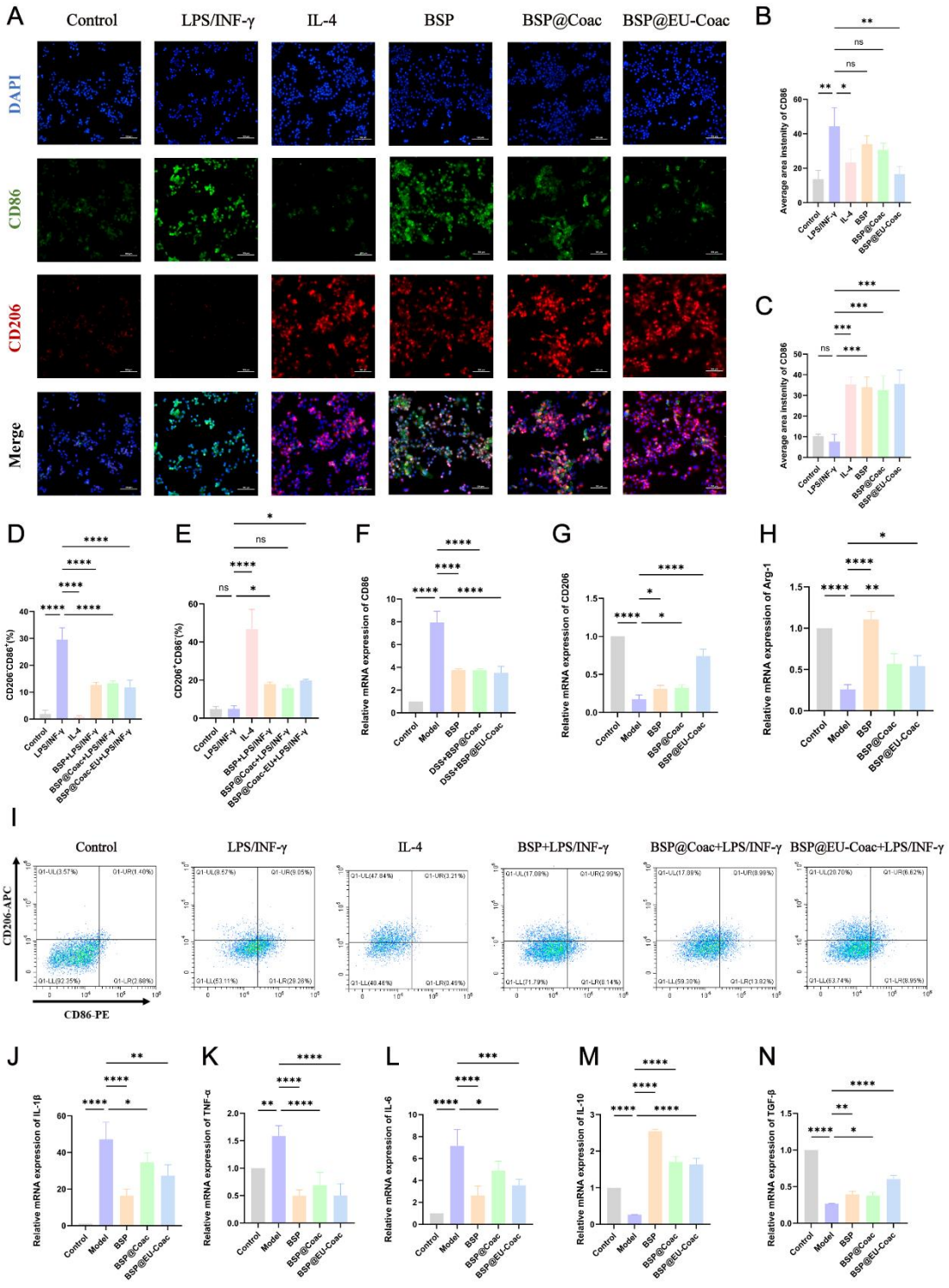

Fig.3 *In vitro* macrophage reprogramming by BSP-loaded coacervates (A-C) Representative immunofluorescence images and corresponding quantitative analysis in RAW 264.7. (I, D, E) Representative flow cytometry plots and quantitative analysis of the pro-inflammatory M1 ($CD86^{+}CD206^{-}$) and reparative M2 ($CD86^{-}CD206^{+}$). (F-N) Relative mRNA expression levels of M1-associated (CD86, IL-1β, TNF-α, IL-6) and

M2-associated (CD206, Arg-1, IL-10, TGF-β) genes in BMDMs assessed by qRT-PCR. Data are represented as mean values ± SD (n=3). *$p < 0.05$, **$p < 0.01$, ***$p < 0.001$.

3.8 BSP@EU-Coac Reprograms Macrophages to Improve Inflammatory Microenvironment

Macrophages serve as principal immunomodulatory mediators during the inflammatory and reparative phases of intestinal diseases. In the destructive microenvironment of colitis, the polarization transition from the pro-inflammatory M1 phenotype to the reparative M2 phenotype is severely impaired, perpetuating inflammatory cascades and chronic mucosal damage. Consequently, this study investigated the in vitro regulatory effects of the developed delivery systems on macrophage polarization to evaluate their potential for immune microenvironment reprogramming. To comprehensively and rigorously assess phenotypic transitions, we utilized RAW 264.7 cells for morphological evaluation alongside primary bone marrow-derived macrophages (BMDMs) for flow cytometric and transcriptomic quantitative analyses. Immunofluorescence assays on RAW 264.7 cells (Fig. 3A–C) visually demonstrated that LPS/IFN-γ stimulation induced robust expression of CD86 (green, M1 marker), whereas IL-4 induction resulted in strong CD206 (red, M2 marker) positivity. Quantitative analysis confirmed that treatment with BSP@EU-Coac significantly attenuated the expression of the M1 marker while concurrently elevating the fluorescence intensity of the M2 marker.

Flow cytometry conducted on primary BMDMs further validated these phenotypic shifts with high precision (Fig. 3I, D, E). LPS/IFN-γ stimulation successfully induced a pro-inflammatory state, surging the proportion of $CD86^{+}CD206^{-}$ M1 macrophages to 29.26%. In stark contrast, BSP@EU-Coac treatment exerted exceptional repolarization efficacy, profoundly reducing this pro-inflammatory subpopulation to 8.95%. Concomitantly, the proportion of $CD86^{-}CD206^{+}$ M2 macrophages was elevated to 20.70%, demonstrating an immunomodulatory trend highly consistent with the IL-4-induced positive control.

Furthermore, qRT-PCR analysis of BMDMs corroborated this reprogramming at the transcriptomic level. Compared to the Model (LPS/IFN-γ) group, the administration of BSP@EU-Coac significantly downregulated the relative mRNA expression of distinct M1 markers (CD86, IL-1β, TNF-α, IL-6) (Fig. 3F, J–L), while markedly upregulating M2-associated genes (CD206, Arg-1, IL-10, TGF-β) (Fig. 3G, H, M, N). Taken together, these multidimensional results compellingly demonstrate that the enteric-coated coacervate system efficiently suppresses M1 pro-inflammatory polarization and potently drives the transition of macrophages toward a reparative M2 phenotype.

3.9 Therapeutic Evaluation of BSP@EU-Coac In Vivo

In this study, we utilized a mouse model of UC induced by DSS to explore the therapeutic effect of BSP@EU-Coac. We also used first-line clinical drug 5-aminosalicylic acid (5-ASA), as a positive control. We conducted the animal modeling and administration according to Fig. 4A. As anticipated, the DSS-challenged Model group exhibited a dramatic body weight loss of up to 4.62±1.33 g and peaked DAI scores by day 7. This was accompanied by significant colon shortening compared with the Control group (4.99±1.23 cm), indicating the successful establishment of severe colonic inflammation (Fig. 4L, M). Specifically, the BSP@EU-Coac group exhibited the most rapid body weight recovery, the lowest DAI scores, and the most effective preservation of colon length, significantly outperforming the unencapsulated BSP and comparable to or exceeding the efficacy of 5-ASA. In terms of weight change, the body weight of mice in the BSP@EU-Coac group ceased to decrease from day 8, and exhibited a steady recovery, whereas the other treatment groups showed negligible rebound trends (Fig. 4B). Furthermore, BSP@EU-Coac treatment significantly improved colon length (8.66±1.92 cm), which is significantly better than the other groups. There were similar differences in weight changes and DAI scores, indicating that BSP@EU-Coac had a certain relieving effect on UC symptoms in mice (Fig. 4C).

The DSS-induced systemic immune response was evidenced by marked splenomegaly (increased spleen index) and aberrant hematological profiles, including

elevated white blood cell (WBC) and neutrophil (NEUT) counts, alongside depleted lymphocytes (LYMPH) (Fig. 4D–F). Treatment with BSP@EU-Coac effectively normalized these systemic inflammatory parameters. Furthermore, biochemical analyses of hepatic and renal function (ALT, AST, BUN) and the liver index revealed that the DSS-induced mild organ stress was mitigated by BSP@EU-Coac, confirming that the enteric-coated coacervate system exhibits excellent systemic biocompatibility without eliciting off-target toxicity (Fig. 4G–I, S4A). Beyond local intestinal healing, we evaluated the systemic biosafety of BSP@EU-Coac. The DSS-induced systemic inflammation, evidenced by significant splenomegaly (Fig. 4K), was effectively normalized by BSP@EU-Coac treatment. Furthermore, the mass indices of the liver (Fig. 4J), heart, lungs, and kidneys (Fig. S3 B-D) exhibited no significant fluctuations across all groups.

To further explore the extent of damage to colon tissue and the effects of treatment, H&E and AB-PAS sections were analyzed. As shown in Fig. 4N, the control group did not exhibit significant ulceration, colon injury, or inflammatory cells infiltration in the colon region. Conversely, the model group displayed severe colonic tissue edema, ulcerated area, inflammatory cells infiltration and disappearance of U-shaped crypts. Compared with the model group, the severity of inflammation slightly decreased in the free BSP, BSP@Coac, and 5-ASA group. In the BSP@EU-Coac treated mice, there was no apparent inflammatory damage, with a complete crypt structure similar to the control, which indicated that BSP@EU-Coac had good therapeutic effect on UC. Furthermore, we conducted histopathological evaluations of vital organs—including the heart, liver, spleen, lungs, and kidneys—using hematoxylin and eosin (H&E) staining (Fig. S4). No discernible histopathological abnormalities or lesions were observed in the organ sections across the experimental groups. These findings further corroborate the excellent *in vivo* biocompatibility and systemic safety profile of the BSP@EU-Coac delivery system. Additionally, Alcian Blue staining, which highlights mucin-secreting goblet cells, demonstrated severe mucin depletion in the DSS group. Remarkably, the BSP@EU-Coac group exhibited a nearly complete restoration of goblet cell abundance and mucin production, maintaining the integrity of the protective mucosal barrier.

Collectively, these in vivo results underscore the superior targeted anti-inflammatory and mucosal healing capabilities of the BSP@EU-Coac system.

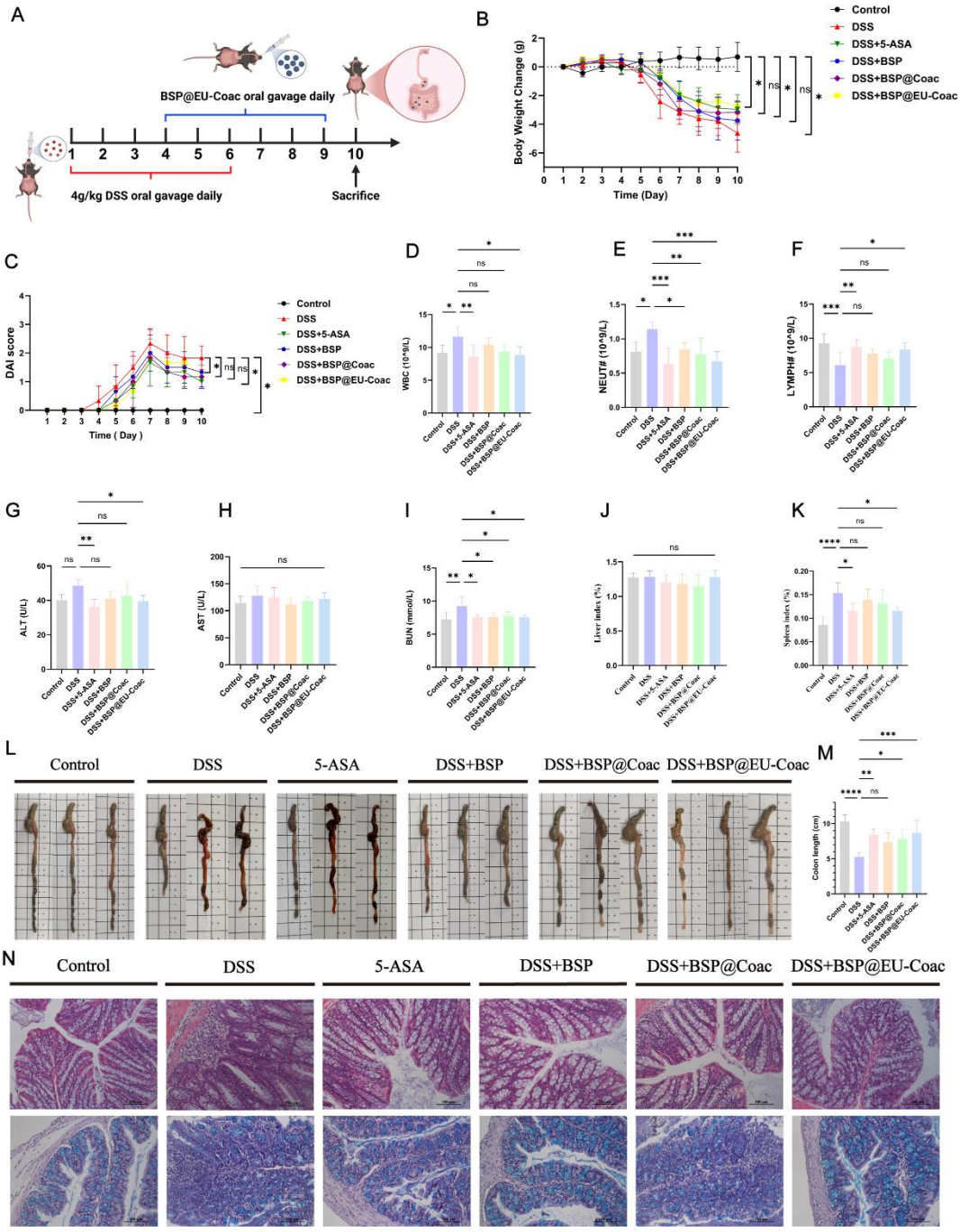

Fig.4 *In vivo* therapeutic efficacy and systemic biosafety of BSP@EU-Coac in a DSS-induced colitis mouse model. (A) Schematic illustration of the experimental design for colitis induction and the subsequent oral administration protocol. (B, C) Daily monitoring of body weight changes and DAI scores. (L, M) Representative macroscopic images of the excised colons and the corresponding quantitative analysis

of colon length at the experimental endpoint. (D-F) Hematological profiling evaluating the systemic immune response, including WBC, NEUT, and LYMPH counts. (G-I) Serum biochemical analysis assessing hepatic and renal functions: ALT, AST, and BUN. (J, K) Organ indices of the liver and spleen. (N) Representative H&E (top row) and AB-PAS (bottom row) staining images of colonic sections from different treatment groups. Data are represented as mean values ± SD (n=6). *$p < 0.05$, **$p < 0.01$, ***$p < 0.001$.

3.10 In Vivo Biodistribution and Inflamed Colon Targeting of FBSP@EU-Coac

To investigate whether the enteric-coated coacervate system could facilitate site-specific delivery and prolonged retention in the diseased colonic milieu, we systematically monitored the spatiotemporal distribution of 5-DTAF-labeled formulations in a DSS-induced murine colitis model (Fig. 5A). Upon oral gavage, in vivo bioluminescence imaging revealed that free 5-DTAF and naked FBSP were rapidly cleared from the gastrointestinal (GI) tract, with fluorescence signals significantly dissipating within 6 h (Fig. 5B). Although the FBSP@Coac group showed moderate retention, it lacked the precision required for colonic targeting, as evidenced by the diffused signal across the upper GI tract. In stark contrast, the FBSP@EU-Coac group exhibited a distinct and robust fluorescence signal that progressively transitioned toward the lower abdomen and persisted for up to 24 h post-administration (Fig. 5B, D). The ex vivo fluorescence analysis of harvested GI tracts further corroborated the superior targeting efficiency of the enteric-functionalized system. As illustrated in Fig. 5C, the Eudragit S100 coating effectively shielded the coacervate core from the harsh acidic environment of the stomach, enabling the intact delivery of FBSP to the colonic lesions. Notably, while other formulations showed negligible presence in the colon by 12 h, FBSP@EU-Coac demonstrated selective colonization and intensified accumulation at the inflamed sites (Fig. 5C, E).

The fluorescence distribution in major organs was further examined (Fig. S5 A-C).

Across all experimental groups, fluorescence signals were predominantly enriched in the liver and kidneys, identifying these organs as the primary sites for the systemic uptake, metabolism, and elimination of BSP derivatives. In the Free 5-DTAF group, the liver and kidneys exhibited prominent signals that peaked at 1 h and gradually attenuated thereafter, whereas the other groups reached their maximum signal intensity at 6 h post-administration. Crucially, distinct from the rapid systemic influx and distribution observed in the Free 5-DTAF and FBSP groups, the FBSP@EU-Coac group demonstrated a more controlled and attenuated organ distribution profile. This indicates that the pH-responsive enteric coating effectively sequesters the majority of the payload within the gastrointestinal tract, thereby minimizing premature entry into the systemic circulation and reducing potential off-target effects. This metabolic signature is consistent with the pharmacokinetic behavior of other high-molecular-weight natural polysaccharides[32, 33], further corroborating the superior biosafety and site-specific targeting advantages of the coacervate delivery system developed in this study.

Quantitative analysis confirmed that the fluorescence intensity of the FBSP@EU-Coac group in the colonic region was significantly higher than that of the other three groups at all tested time points. These findings indicate that the pH-responsive EU S100 shell not only prevents premature drug release in the stomach and small intestine but also synergizes with the mucoadhesive properties of the coacervate core to achieve "precision-guided" delivery and sustained retention within the colonic inflammatory microenvironment.

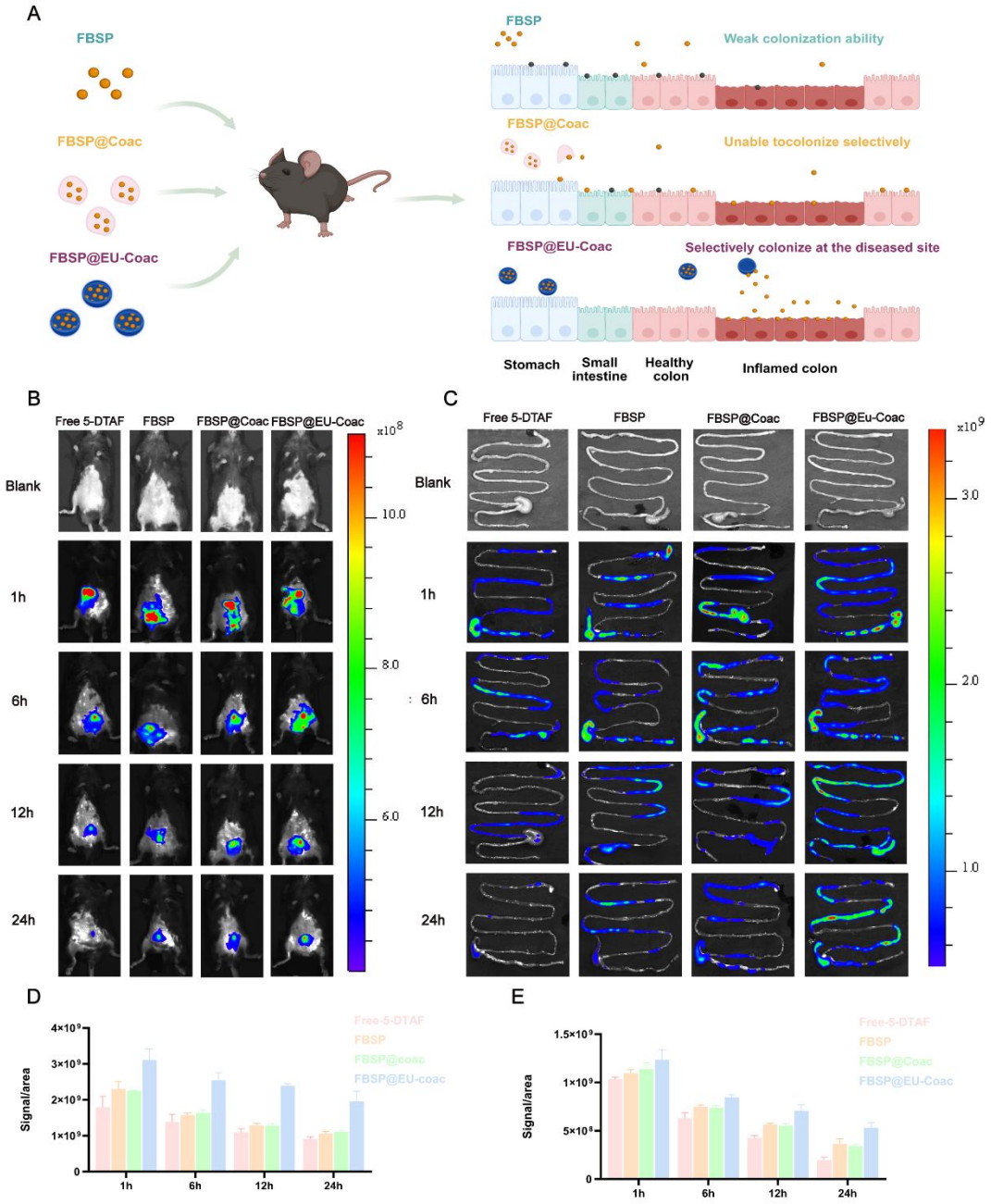

Fig.5 *In vivo* biodistribution and targeted colonic retention of the coacervates. (A) Schematic illustration of the oral administration and gastrointestinal transit of the fluorescently labeled formulations. (B, C) Representative *in vivo* whole-body fluorescence images of DSS-induced colitis mice and ex vivo fluorescence images of their excised gastrointestinal tracts at predetermined time points (1, 6, 12, and 24 h) following oral administration of free 5-DTAF, FBSP, FBSP@Coac, and FBSP@EU-Coac. Blank represents untreated mice. (D, E) Corresponding quantitative analysis of the region-of-interest (ROI) fluorescence intensity (Signal/area) derived

from the in vivo and ex vivo imaging. Data are represented as mean values ± SD (n=3). *$p < 0.05$, **$p < 0.01$, ***$p < 0.001$.

3.11 In Vivo Modulation of Macrophage Polarization and Amelioration of Colonic Oxidative Stress

To elucidate the underlying immunomodulatory mechanisms driving the therapeutic efficacy of BSP@EU-Coac, we investigated macrophage polarization within the inflamed colonic mucosa. During colitis progression, the disruption of intestinal homeostasis triggers massive infiltration of pro-inflammatory M1 macrophages, which perpetuate tissue damage[34]. Immunofluorescence co-staining (Fig. 6A) revealed a substantial accumulation of general macrophages ($F4/80^+$) and a predominant polarization towards the pro-inflammatory M1 phenotype ($CD86^+$) in the DSS-induced Model group. Consistent with our in vitro findings, treatment with BSP@EU-Coac significantly suppressed overall macrophage infiltration (Fig. 6B) and drastically attenuated CD86 expression (Fig. 6C). Conversely, evaluation of the reparative M2 macrophage population (F4/80+/CD206+) demonstrated that while DSS challenge severely depleted M2 macrophages, oral administration of BSP@EU-Coac markedly upregulated CD206 expression in the colonic lamina propria (Fig. 6D–F). qRT-PCR analysis of the colonic tissues also confirmed that BSP@EU-Coac significantly downregulated the mRNA expression of CD86 (Fig. 6G) while potently upregulating the reparative marker CD206 (Fig. 6H). Furthermore, the aberrant activation of M1 macrophages in colitis is intrinsically linked to severe localized oxidative stress, which further exacerbates epithelial barrier dysfunction[35]. Therefore, we assessed colonic redox homeostasis by quantifying key oxidative and antioxidant markers. As anticipated, DSS induction resulted in a dramatic accumulation of malondialdehyde (MDA), a hallmark of lipid peroxidation (Fig. 6J), alongside a concurrent depletion of critical endogenous antioxidants, including glutathione (GSH, Fig. 6I) and superoxide dismutase (SOD, Fig. 6K). Remarkably, BSP@EU-Coac treatment effectively reversed these oxidative impairments. Collectively, these in vivo

findings compellingly demonstrate that the enteric-coated coacervate system orchestrates mucosal healing by synergistically reprogramming macrophages towards a reparative phenotype and re-establishing the intestinal redox balance.

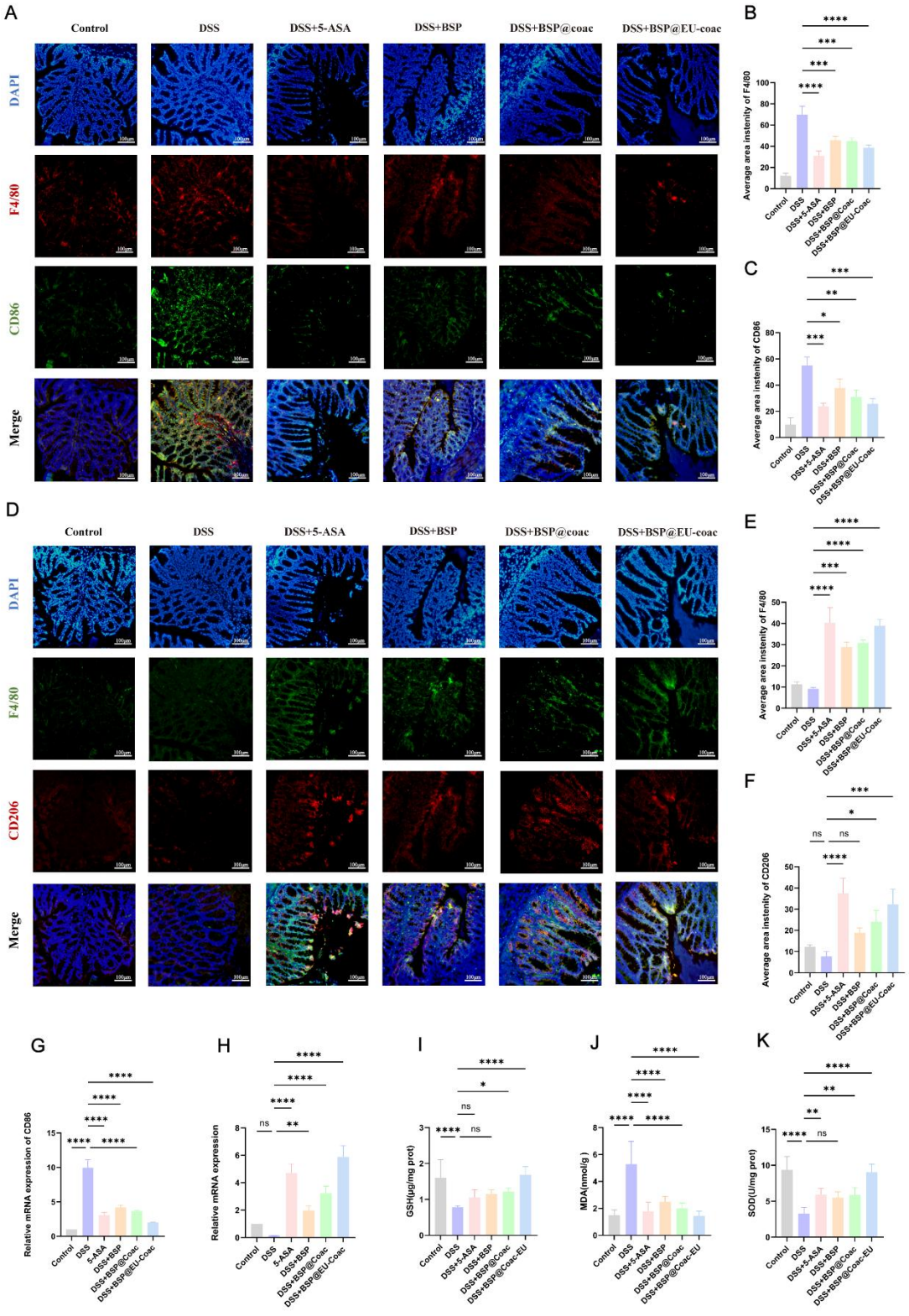

Fig.6 *In vivo* modulation of colonic macrophage polarization and amelioration of

oxidative stress by BSP@EU-Coac. (A, D) Representative immunofluorescence images of colonic tissues co-stained for DAPI (blue), the pan-macrophage marker F4/80 (red or green), and the M1 marker CD86 (green) or the M2 marker CD206 (red). (B-C, E-F) Corresponding quantitative analysis of the average fluorescence area intensity for F4/80, CD86, and CD206 in the colonic lamina propria. (G, H) Relative mRNA expression levels of the pro-inflammatory marker CD86 and the reparative marker CD206 in colonic tissues determined by qRT-PCR. (I-K) Quantification of colonic redox homeostasis markers, including glutathione (GSH), malondialdehyde (MDA), and superoxide dismutase (SOD). Data are represented as mean values ± SD (n=6). *$p < 0.05$, **$p < 0.01$, ***$p < 0.001$.

3.12 Evaluation on Repairing Colonic Epithelial Barrier Function of BSP@EU-Coac

Studies have shown that intestinal epithelial barrier dysfunction is a crucial factor contributing to the occurrence and progression of UC. Tight junction proteins are integral components of the intestinal epithelial barrier, which regulate the selective permeability of the barrier, prevent the invasion of harmful bacteria and toxins into the mucosal layer, and thereby avoid triggering intestinal and systemic inflammation[36]. Given the severe barrier compromise observed in ulcerative colitis, we evaluated the restorative efficacy of BSP@EU-Coac on the epithelial architecture. Immunofluorescence co-staining (Fig. 7A, B) revealed that DSS induction led to a profound depletion and discontinuous distribution of TJ proteins (ZO-1, Occludin, Claudin-1) as well as the major goblet cell-derived mucin (Muc-2). Remarkably, oral administration of BSP@EU-Coac robustly rescued the structural continuum of these barrier-forming proteins, displaying dense and organized fluorescence networks comparable to those of the healthy control. Quantitative analysis of the fluorescence area (Fig. 7D–G) corroborated that BSP@EU-Coac treatment significantly enhanced the protein-level expression of TJs and Muc-2. Furthermore, the regenerative capacity of the epithelium was assessed using the cellular proliferation marker Ki67[37] (Fig. 7C,

H). The BSP@EU-Coac group exhibited a substantial accumulation of Ki67+ proliferating cells predominantly localized within the colonic crypts, indicative of accelerated re-epithelialization and active mucosal healing.

qRT-PCR analysis also demonstrated that BSP@EU-Coac significantly upregulated the mRNA expression of Claudin-1, Occludin and ZO-1 (Fig. 7I–K) compared to the DSS-challenged mice. Since epithelial barrier repair is intricately coupled with the resolution of underlying mucosal inflammation, we further profiled the local cytokine milieu. Consistent with the macrophage repolarization data, BSP@EU-Coac treatment nearly abrogated the DSS-induced transcriptomic storm of TNF-α, IL-6 and IL-1β (Fig. 7L–N). Concurrently, it substantially boosted the expression of tissue-repairing and anti-inflammatory cytokines including IL-10 and TGF-β (Fig. 7O–P). Collectively, these findings provide compelling evidence that the targeted delivery of BSP@EU-Coac orchestrates comprehensive mucosal healing by reinforcing tight junction assembly, stimulating crypt cell proliferation, and reprogramming the local microenvironment towards a pro-resolving state.

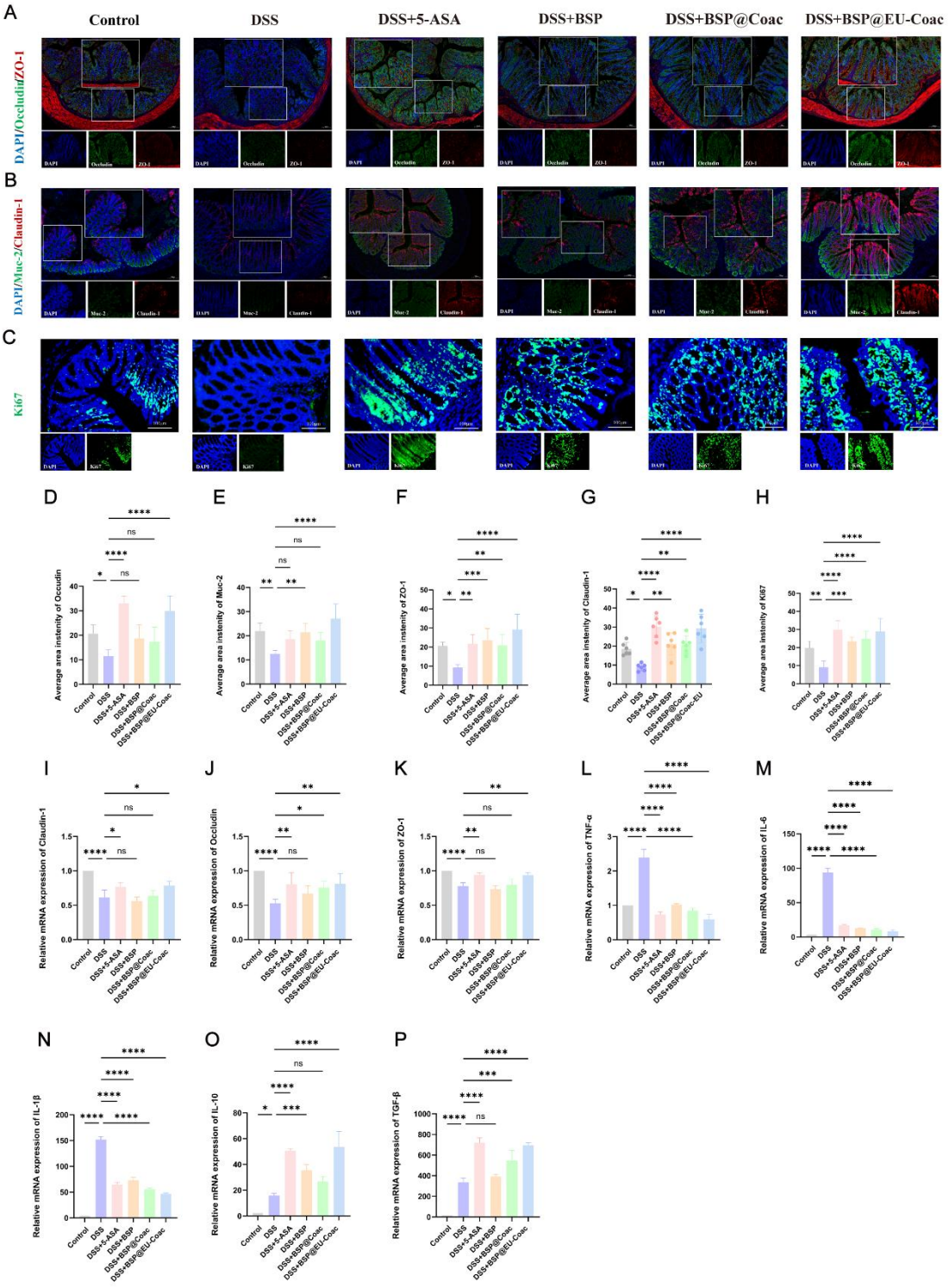

Fig.7 Restoration of the colonic epithelial barrier and modulation of the mucosal cytokine milieu by BSP@EU-Coac. (A, B) Representative immunofluorescence co-staining images of colonic sections illustrating the distribution of tight junction proteins and mucin: Occludin (green) and ZO-1 (red), and Muc-2 (green) and Claudin-1 (red). (C) Immunofluorescence staining for the cellular proliferation marker Ki67 (green) in

colonic crypts. Nuclei were counterstained with DAPI (blue). (D-H) Corresponding quantitative analysis of the average fluorescence area intensity for Occludin, Muc-2, ZO-1, Claudin-1, and Ki67. (I-K) Relative mRNA expression levels of epithelial barrier-associated genes, including Claudin-1, Occludin, and ZO-1, assessed by qRT-PCR. (L-P) Transcriptomic quantification of colonic pro-inflammatory (TNF-α, IL-6, IL-1β; l–n) and tissue-repairing anti-inflammatory (IL-10, TGF-β; o, p) cytokines. Data are represented as mean values ± SD (n=6). *$p < 0.05$, **$p < 0.01$, ***$p < 0.001$.

3.13 Effects of BSP@EU-Coac on the Balance of Intestinal Microbiota

Gut microbiota homeostasis is essential for gut health, and gut microbiota disorders can lead to and aggravate the symptoms of UC[38, 39]. Therefore, in this study, we used 16S rDNA gene sequencing to investigate the changes in the composition and abundance of intestinal flora caused by indicated BSP-formulations. Our results, shown in Fig. 8a, indicated that the Control, Model, and BSP@EU-Coac groups possessed 127, 158, and 172 unique exact amplicon sequence variants (ASVs), respectively, with 80 ASVs shared among all groups, demonstrating that the microbial community structures were distinctly altered. We further evaluated the alpha diversity of the intestinal flora. While the community richness (Chao index, Fig. 8B) showed slight fluctuations, the community diversity and evenness (Simpson and Shannon indices, Fig. 8C, D) were significantly reshaped following BSP@EU-Coac treatment compared to the model group. To further analyze the similarity and difference among the groups, we used principal coordinate analysis (PCoA) and cluster analysis. In the PCoA, closer sample distances indicate greater similarity in microbial composition structure between samples. As shown in Fig. 8E, F, there was a distinct spatial separation between the Control and Model groups, representing severe DSS-induced dysbiosis. Notably, the BSP@EU-Coac treated group formed a distinct cluster separate from the Model group, indicating a significant structural divergence and reshaping of the flora. Additionally, the difference between the groups was significantly greater than that of the samples

within each group, making the comparison between groups meaningful. Next, we conducted a thorough analysis of the species and abundance of intestinal bacteria in each group at the genus level. As illustrated in the community barplot and heatmap (Fig. 8G, H), the DSS-induced Model group exhibited aberrant expansions of specific taxa, whereas treatment with BSP@EU-Coac led to an improvement in species composition and effectively restructured the microbial distribution. Finally, to rigorously identify the specific bacterial taxa driving these compositional differences, we performed Linear discriminant analysis Effect Size (LEfSe) (Fig. 8I, J). The Model group was characterized by a pathological enrichment of opportunistic pathogens such as Escherichia-Shigella and Turicibacter. Conversely, various treatments reversed these changes, and the BSP@EU-Coac group had a particularly strong regulatory effect, resulting in a higher amount of beneficial probiotics, most notably *Akkermansia* and *Romboutsia* (LDA score> 3.0). Notably, *Akkermansia muciniphila*, a mucin-degrading bacterium residing in the intestinal mucus layer, has emerged as a crucial regulator of host physiology with significant implications for health and disease. Accumulating evidence indicates that it enhances intestinal barrier integrity, modulates microbial composition, and regulates immune responses[40, 41]. Similarly, *Romboutsia* is widely recognized as a beneficial short-chain fatty acid (SCFA)-producing commensal that contributes to the maintenance of a healthy colonic mucosa and the suppression of local inflammation[42]. In conclusion, BSP@EU-Coac was able to alleviate UC by restoring intestinal flora homeostasis and enriching beneficial bacteria.

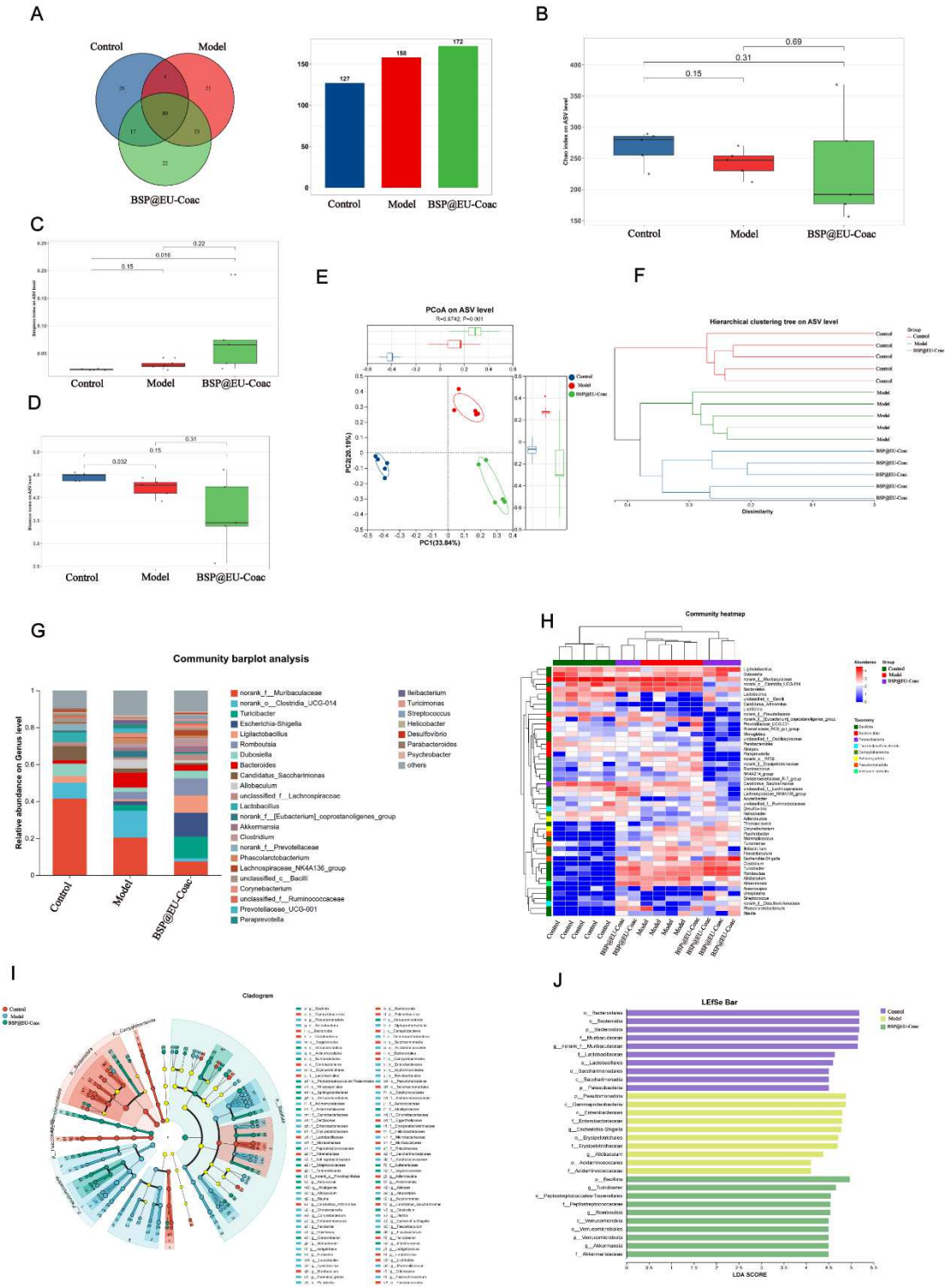

Fig.8 BSP@EU-Coac alleviates DSS-induced colitis by restoring gut microbiota homeostasis. (A) Venn diagram illustrating the unique and shared exact ASVs among the Control, Model, and BSP@EU-Coac groups. (B-D) Alpha diversity analysis of the gut microbiota, showing the Chao1 richness index, Simpson index, and Shannon index. (E) PCoA plot based on ASV levels, depicting the beta diversity and spatial separation of the microbial communities. (F) Hierarchical clustering tree demonstrating the

similarity of microbial compositions across different samples. (G) Relative abundance of the dominant gut microbiota at the genus level. (H) Community heatmap illustrating the hierarchical clustering of differential genera across all biological replicates. (I-J) LEfSe identifying the specific predictive bacterial biomarkers for each group. Data are represented as mean values ± SD (n=5). *$p < 0.05$, **$p < 0.01$, ***$p < 0.001$.

4. Conclusion

In summary, we engineered an orally administered, enteric-coated coacervate system (BSP@EU-Coac) to overcome the limitations of conventional monotherapies in treating UC. By achieving precise spatiotemporal delivery to inflamed colonic lesions, BSP@EU-Coac acts as a potent ROS scavenger, which directly drives the reprogramming of macrophages from a tissue-destructive M1 state to a pro-resolving M2 phenotype. This redox and immune restoration creates a permissive microenvironment for deep mucosal healing and fortifies the physical epithelial barrier. Crucially, this targeted delivery fundamentally reshapes host-microbiome symbiosis by suppressing opportunistic pathogens and enriching beneficial commensals like *Akkermansia*. By seamlessly integrating targeted drug delivery, redox restoration, immune reprogramming, barrier fortification, and microbiota restructuring into a single nanotherapeutic platform, BSP@EU-Coac fundamentally breaks the pathological cycle of UC, offering a highly translatable strategy for long-term remission.

Declarations:

Ethical Approval

This study was conducted according to the guidelines of the National Institutes of Health Guide for the Care and Use of Laboratory Animals (NIH Publications No. 8023, revised 1978), and it was approved by the Ethics Committee of Animal Experiments Center of Zhejiang Chinese Medical University (protocol code is IACUC- 20250616-10).

ARRIVE guidelines

We confirm that study was reported in accordance with ARRIVE guidelines.

Consent to Participate

Not applicable.

Consent to Publish

Not applicable.

CRediT authorship contribution statement

Qiantao Zhang.: Data curation, Writing - original draft, Visualization**.** Lai Chai.: Formal analysis, Investigation. Hui Liu.: Formal analysis, Investigation. Xueer Hu.: Formal analysis, Investigation, Writing - original draft. Yujing Niu.: Investigation, Methodology. Hongli Cao.: Project administration, Software. Xin Rao.: Project administration, Software. Mingyuan Zhou.: Project administration, Software. Yuchi Chen.: Project administration, Software. Xiaoqing Ye.: Project administration, Software. Fangmei Zhou.: Supervision, Validation. Bingqi Zhu. and Zhishan Ding.: Funding acquisition, Writing - review & editing.

Funding

This work was supported by The National Natural Science Foundation of China (Grant

No. 82374127), the Research Project of Zhejiang Chinese Medical University (2025JKZKTS27), Zhejiang Medical Science and Technology Program (Grant number 2025696139).

Competing Interests

The authors declare no competing financial interest.

Data availability

All data generated or analyzed during this study are included in this published article and its supplementary information files.

Acknowledgments

We appreciate the great experimental support from the Medical Research Center, Academy of Chinese Medical Sciences, Zhejiang Chinese Medical University.

References:

[1] H. Cruz, P. Shah, N. Wohlgemuth, R. Ketchum, I. Nassif, C.-A.A. Hu, Pyroptosis in ulcerative colitis: biomarkers and therapeutic targets, Journal of Biomedical Science, 32 (2025) 106. DOI: https://doi.org/10.1186/s12929-025-01206-x.

[2] P. Wangchuk, K. Yeshi, A. Loukas, Ulcerative colitis: clinical biomarkers, therapeutic targets, and emerging treatments, Trends in Pharmacological Sciences, 45 (2024) 892-903. DOI: https://doi.org/10.1016/j.tips.2024.08.003.

[3] D.T. Rubin, A.N. Ananthakrishnan, C.A. Siegel, E.L. Barnes, M.D. Long, ACG Clinical Guideline Update: Ulcerative Colitis in Adults, Official journal of the American College of Gastroenterology | ACG, 120 (2025). DOI: https://doi.org/10.14309/ajg.0000000000003463.

[4] N. Krugliak Cleveland, J. Torres, D.T. Rubin, What Does Disease Progression Look Like in Ulcerative Colitis, and How Might It Be Prevented?, Gastroenterology, 162 (2022) 1396-1408. DOI: https://doi.org/10.1053/j.gastro.2022.01.023.

[5] M.F. Neurath, M. Vieth, Different levels of healing in inflammatory bowel diseases: mucosal, histological, transmural, barrier and complete healing, Gut, 72 (2023) 2164. DOI: https://doi.org/10.1136/gutjnl-2023-329964.

[6] Q. Lv, H. Yang, Y. Xie, X. Huang, Z. Yan, Y. Lv, Y. Cui, L. Hu, H. Qiao, Prunus mume derived extracellular vesicle-like particles alleviate experimental colitis via disrupting NEK7-NLRP3 interaction and inflammasome activation, Journal of Nanobiotechnology, 23 (2025) 532. DOI: https://doi.org/10.1186/s12951-025-03567-9.

[7] F.-H. Wei, W.-Y. Xie, P.-S. Zhao, Z.-H. Ji, F. Gao, C.-Z. Chen, Z. Zhang, W. Gao, B. Yuan, Crataegus pinnatifida polysaccharide alleviates DSS-induced colitis in mice by regulating the intestinal microbiota and enhancing arginine biosynthesis, Phytomedicine, 142 (2025) 156794. DOI: https://doi.org/10.1016/j.phymed.2025.156794.

[8] H. Hou, L. Li, T. Islam, J. Shi, M. Hou, S. Jiang, X. Zhao, C. Lin, Q. Han, L. Zhu, Z. Bian, Precise structural characterization and therapeutic potential of a glucomannan polysaccharide from dried rhizome of plant Bletilla striata against ulcerative colitis, Carbohydrate Polymers, 380 (2026) 125038. DOI: https://doi.org/10.1016/j.carbpol.2026.125038.

[9] B. Wang, C. Wu, Y. Ma, X. Liu, L. Tao, X. Zhou, L. Jia, Recent advances in Bletilla striata polysaccharide research: extraction methodologies, structural elucidation, pharmacological mechanisms, structure–activity relationships, and therapeutic delivery applications, Volume 16 - 2025 (2025). DOI: https://doi.org/10.3389/fphar.2025.1688676.

[10] N. Cao, Zhao, Z., Zhao, Y. T., et al., Degradation of Poria cocos polysaccharides in simulated gastric juice and intestinal juice and its intestinal absorption in vivo., Science and Technology of Food Industry, 41 (2020) 61-67. DOI: https://doi.org/10.13386/j.issn1002-0306.2019100063.

[11] B. Ding, W. Jiang, T. Ouyang, H. Xu, Smart coacervate microdroplets: biomimetic design, material innovations, and emerging applications in biomacromolecule delivery, Bioactive Materials, 52 (2025) 244-270. DOI: https://doi.org/10.1016/j.bioactmat.2025.06.016.

[12] J. Lim, S. Gudlur, C. Buchanan, Q.M. Perrin, H. Boyd, M. Moulin, H. Iwase, L. Porcar, M. Cárdenas, A. Miserez, K. Pervushin, Hierarchical Structural Organization in Bioinspired Peptide Coacervate Microdroplets, ACS Nano, 19 (2025) 35724-35739. DOI: https://doi.org/10.1021/acsnano.5c12015.

[13] L. Jia, C. Zhou, Y. Qiao, Enzymatically reconfigurable liquid crystalline coacervate microdroplets as protocell models, Nature Communications, 16 (2025) 10554. DOI: https://doi.org/10.1038/s41467-025-65601-6.

[14] Z. Zhang, Y. Pan, X. Fan, N. Du, Q. Pan, L. Ye, X. Ding, P. Cai, K. Luo, B. Hu, B. He, Y. Pu, A Colon-Targeted Oral Nanosystem Disrupts the Inflammatory Loop in Enteric Glia to Alleviate Ulcerative Colitis, ACS Nano, 19 (2025) 28242-28256. DOI: https://doi.org/10.1021/acsnano.5c05032.
[15] C. Chen, L. Guilbaud, V. Marotti, W. Zhang, I. Domingues, H. Yagoubi, K. Vints, Y. Xu, A. Beloqui, An antioxidant metal-organic framework with functional coatings for oral anti-TNF-α antibody delivery in inflammatory bowel disease treatment, Journal of Controlled Release, 389 (2026) 114411. DOI: https://doi.org/10.1016/j.jconrel.2025.114411.
[16] Y. Tian, Q. Hu, Z. Sun, Y. Yu, X. Li, T. Tian, X. Bi, Y. Li, B. Niu, Z. Zhang, Colon Targeting pH-Responsive Coacervate Microdroplets for Treatment of Ulcerative Colitis, Small, 20 (2024) 2311890. DOI: https://doi.org/10.1002/smll.202311890.
[17] C. Shen, F. Zhou, Y. Chen, B. Zhu, Y. Li, Z. Mao, Y. Wang, X. Li, M. Zhou, J. Wu, Z. Ding, Oral absorption, cellular uptake and transport mechanisms of a novel glucuronogalactomannan from Tetrastigma hemsleyanum Diels et Gilg in the intestinal epithelium, Carbohydrate Polymers, 380 (2026) 125023. DOI: https://doi.org/10.1016/j.carbpol.2026.125023.
[18] Z. Zheng, Y. Zhang, Y. Liu, J. Wang, Z. Cui, X. Pan, Y. Liu, W. Tang, K. Wang, Metabolic degradation of lentinan in liver mediated by CYP450 enzymes and epoxide hydrolase, Carbohydr Polym, 253 (2021) 117255. DOI: https://doi.org/10.1016/j.carbpol.2020.117255.
[19] X. Liu, N. Quan, Immune Cell Isolation from Mouse Femur Bone Marrow, Bio-protocol, 5 (2015) e1631. DOI: https://doi.org/10.21769/BioProtoc.1631.
[20] Y. Niu, H. Cao, Q. Zhang, X. Rao, L. Chai, X. Hu, F. Zhou, M. Zhou, Y. Chen, X. Ye, Y. Shen, Z. Ding, B. Zhu, Self-assembled nanozyme-functionalized dynamic double-network hydrogel accelerates diabetic wound repair by remodeling the immune microenvironment and promoting vascular-nerve regeneration, Chemical Engineering Journal, 535 (2026) 175155. DOI: https://doi.org/10.1016/j.cej.2026.175155.
[21] J. Li, X. Jiang, Y. Duan, X. Li, J. Dong, B. Yang, Y. Li, Stable Coacervate Microdroplets as Robust Microreactors for Enhanced Enzymatic Catalysis, Small, 22 (2026) e14871. DOI: https://doi.org/10.1002/smll.202514871.
[22] Y. Liu, A.L. Ahumada, E. Bayraktar, P. Schwartz, M. Chowdhury, S. Shi, M.M. Sebastian, H. Khant, N. de Val, N.N. Bayram, G. Zhang, T.C. Vu, Z. Jie, N.B. Jennings, C. Rodriguez-Aguayo, J. Swain, E. Stur, L.S. Mangala, Y. Wu, S. Nagaraju, B. Ermias, C. Li, G. Lopez-Berestein, J. Braam, A.K. Sood, Enhancing oral delivery of plant-derived vesicles for colitis, Journal of Controlled Release, 357 (2023) 472-483. DOI: https://doi.org/10.1016/j.jconrel.2023.03.056.
[23] Y. Zhang, N. Wu, J. Wang, Z. Chen, Z. Wu, M. Song, Z. Zheng, K. Wang, Gastrointestinal metabolism characteristics and mechanism of a polysaccharide from Grifola frondosa, Int J Biol Macromol, 253 (2023) 126357. DOI: https://doi.org/10.1016/j.ijbiomac.2023.126357.
[24] K. Wang, Y. Liu, Z. Zhang, Z. Zheng, W. Tang, W. Teng, X. Mu, J. Wang, Y. Zhang, Insights into oral lentinan immunomodulation: Dectin-1-mediated lymphatic transport from Peyer's patch M cells to mononuclear phagocytes, Carbohydr Polym, 346 (2024) 122586. DOI: https://doi.org/10.1016/j.carbpol.2024.122586.
[25] Y. Zhang, Y. Wang, Y. Lu, H. Quan, Y. Wang, S. Song, H. Guo, Advanced oral drug delivery systems for gastrointestinal targeted delivery: the design principles and foundations, Journal of Nanobiotechnology, 23 (2025) 400. DOI: https://doi.org/10.1186/s12951-025-03479-8.
[26] K. Bansal, A. Mukharya, A.B. Jindal, Delivery Strategies and Clinical Significance of Oral Colon-targeted Drug Delivery Systems, AAPS PharmSciTech, 27 (2026) 92. DOI:

https://doi.org/10.1208/s12249-026-03348-z.
[27] M.F. Neurath, D. Artis, C. Becker, The intestinal barrier: a pivotal role in health, inflammation, and cancer, The Lancet Gastroenterology & Hepatology, 10 (2025) 573-592. DOI: https://doi.org/10.1016/S2468-1253(24)00390-X.
[28] J. Zhou, M. Li, Q. Chen, X. Li, L. Chen, Z. Dong, W. Zhu, Y. Yang, Z. Liu, Q. Chen, Programmable probiotics modulate inflammation and gut microbiota for inflammatory bowel disease treatment after effective oral delivery, Nature Communications, 13 (2022) 3432. DOI: https://doi.org/10.1038/s41467-022-31171-0.
[29] K.A. Dunleavy, L.E. Raffals, M. Camilleri, Intestinal Barrier Dysfunction in Inflammatory Bowel Disease: Underpinning Pathogenesis and Therapeutics, Digestive Diseases and Sciences, 68 (2023) 4306-4320. DOI: https://doi.org/10.1007/s10620-023-08122-w.
[30] M. Camilleri, Leaky gut: mechanisms, measurement and clinical implications in humans, Gut, 68 (2019) 1516. DOI: https://doi.org/10.1136/gutjnl-2019-318427.
[31] Y. Ma, S. Gou, Z. Zhu, J. Sun, M.-A. Shahbazi, T. Si, C. Xu, J. Ru, X. Shi, R.L. Reis, S.C. Kundu, B. Ke, G. Nie, B. Xiao, Transient Mild Photothermia Improves Therapeutic Performance of Oral Nanomedicines with Enhanced Accumulation in the Colitis Mucosa, Advanced Materials, 36 (2024) 2309516. DOI: https://doi.org/10.1002/adma.202309516.
[32] B. Zhang, M. Liu, G. Liu, D. Li, B. Zhou, Oral absorption mechanism of the polysaccharides from Gastrodia elata Blume base on fluorescence labeling, Food Research International, 144 (2021) 110342. DOI: https://doi.org/10.1016/j.foodres.2021.110342.
[33] C.-Y. Fang, S.-Y. Chen, C.-C. Liao, J.-D. Chen, G.-C. Yen, Fagopyrum esculentum polysaccharides mitigate obesity by reshaping gut microbiota and enhancing lipid metabolism in high-fat diet-fed mice, International Journal of Biological Macromolecules, 322 (2025) 146668. DOI: https://doi.org/10.1016/j.ijbiomac.2025.146668.
[34] J. Du, J. Zhang, L. Wang, X. Wang, Y. Zhao, J. Lu, T. Fan, M. Niu, J. Zhang, F. Cheng, J. Li, Q. Zhu, D. Zhang, H. Pei, G. Li, X. Liang, H. Huang, X. Cao, X. Liu, W. Shao, J. Sheng, Selective oxidative protection leads to tissue topological changes orchestrated by macrophage during ulcerative colitis, Nature Communications, 14 (2023) 3675. DOI: https://doi.org/10.1038/s41467-023-39173-2.
[35] J. Kinchen, H.H. Chen, K. Parikh, A. Antanaviciute, M. Jagielowicz, D. Fawkner-Corbett, N. Ashley, L. Cubitt, E. Mellado-Gomez, M. Attar, E. Sharma, Q. Wills, R. Bowden, F.C. Richter, D. Ahern, K.D. Puri, J. Henault, F. Gervais, H. Koohy, A. Simmons, Structural Remodeling of the Human Colonic Mesenchyme in Inflammatory Bowel Disease, Cell, 175 (2018) 372-386.e317. DOI: https://doi.org/10.1016/j.cell.2018.08.067.
[36] Y. Wu, X. Zhang, X. Liu, Z. Zhao, S. Tao, Q. Xu, J. Zhao, Z. Dai, G. Zhang, D. Han, J. Wang, Galactooligosaccharides and Limosilactobacillus reuteri synergistically alleviate gut inflammation and barrier dysfunction by enriching Bacteroides acidifaciens for pentadecanoic acid biosynthesis, Nature Communications, 15 (2024) 9291. DOI: https://doi.org/10.1038/s41467-024-53144-1.
[37] Y. Wang, Y. Zhou, Q. Wu, Y. Li, Y. Huang, K. Yu, P. Li, Z. Lv, H. Liu, H. Zou, H. Liu, X. Mou, Honeysuckle-Derived Nanovesicles Regulate Gut Microbiota for the Treatment of Inflammatory Bowel Disease, Advanced Science, 12 (2025) e05208. DOI: https://doi.org/10.1002/advs.202505208.
[38] Y. You, T. Xiang, C. Yang, S. Xiao, Y. Tang, G. Luo, Z. Ling, F. Luo, Y. Chen, Interactions between the gut microbiota and immune cell dynamics: novel insights into the gut-bone axis, Gut Microbes, 17 (2025) 2545417. DOI: https://doi.org/10.1080/19490976.2025.2545417.
[39] J. Zhang, J. Yang, J. Luo, W. Wu, H. Luo, W. Wei, H. Lyu, Y. Wang, H. Yi, Y. Zhang, Z. Fan, H. Lyu,

V.P. Kanakaveti, B. Qin, P. Yuan, R. Yang, H. Zhang, T. Zuo, D.W. Felsher, M.-H. Lee, K. Li, Lactobacillus acidophilus potentiates oncolytic virotherapy through modulating gut microbiota homeostasis in hepatocellular carcinoma, Nature Communications, 16 (2025) 3315. DOI: https://doi.org/10.1038/s41467-025-58407-z.

[40] N. Shaheen, W. Khursheed, B. Gurung, S. Wang, Akkermansia muciniphila: A key player in gut microbiota-based disease modulation, Microbiological Research, 301 (2025) 128317. DOI: https://doi.org/10.1016/j.micres.2025.128317.

[41] L. Marcos-Kovandzic, M. Avagliano, M. Ben Khelil, J. Srikanthan, R. Abdallah, V. Petrocelli, J. Rengassamy, A. Alfaro, M. Bied, M. Fidelle, G. Ferrere, R. Daillère, A. Arbab, R. Amine-Hneineh, A. Pages, P. Dartigues, P. Ly, S. Simon, S. Durand, A. Gottschlich, F. Ginhoux, C. Blériot, P. Liu, L. Zhao, L. Creusot, N. Rolhion, L. Derosa, G. Kroemer, L. Menger, S. Kobold, C. Castilla-Llorente, H. Sokol, S. Casola, E. Pasolli, L. Zitvogel, C. Bigenwald, Gut Microbiota Modulation through Akkermansia spp. Supplementation Increases CAR T-cell Potency, Cancer Discovery, 15 (2025) 1905-1926. DOI: https://doi.org/10.1158/2159-8290.CD-24-1230.

[42] M.-h. Qi, H.-y. Zhang, Y.-y. Hou, I.S. Nguepi Tsopmejio, W. Liu, W.-g. Chang, C. Chen, Z. Wang, W. Li, Ginseng-derived GABAFG ameliorates type 2 diabetes mellitus by modulating autophagy-lysosome pathway and gut microbiota, Journal of Advanced Research, 77 (2025) 465-480. DOI: https://doi.org/10.1016/j.jare.2025.01.003.

Supplementary Files

This is a list of supplementary files associated with this preprint. Click to download.

- SupplementaryMaterials.docx